Revision 1

Origin of Monte Rosa whiteschist from in-situ tourmaline and quartz oxygen isotope analysis by SIMS using new tourmaline reference materials

Katharina Marger[(1)], Cindy Luisier[(1)], Lukas P. Baumgartner[(1)], Benita Putlitz[(1)], Barbara L. Dutrow[(1,2)], Anne-Sophie Bouvier[(1)], Andrea Dini[(3)]

(1) Institute of Earth Science, University of Lausanne, CH-1015, Switzerland

(2) Department of Geology and Geophysics, Louisiana State University, Louisiana 70803, USA

(3) Istituto di Geoscienze e Georisorse, Area di Ricerca del CNR, I-56124 Pisa, Italy

Abstract

A series of tourmaline reference materials are developed for in-situ oxygen isotope analysis by secondary ion mass spectrometry (SIMS), which allow to study the tourmaline compositions found in most igneous and metamorphic rocks. The new reference material was applied to measure oxygen isotope composition of tourmaline from metagranite, meta-leucogranite and whiteschist from the Monte Rosa nappe (Western Alps). The protolith and genesis of whiteschist is highly debated in the literature. Whiteschists occur as 10 to 50 meters tube-like bodies within the Permian Monte Rosa granite. They consist of chloritoid, talc, phengite and quartz, with local kyanite, garnet, tourmaline and carbonates.

Whiteschist tourmaline is characterized by an igneous core and a dravitic overgrowth (X_{Mg} > 0.9). The core reveals similar chemical composition and zonation as meta-leucogranitic tourmaline (X_{Mg}: 0.25, $\delta^{18}O$: 11.3-11.5‰), proving their common origin. Dravitic overgrowths in whiteschists have lower oxygen isotope compositions (8.9-9.5‰). Tourmaline in metagranite is an intermediate schorl-dravite with X_{Mg} of 0.50. Oxygen isotope data reveal homogeneous composition for metagranite and meta-leucogranite tourmalines of 10.4-11.3‰ and 11.0-11.9‰, respectively. Quartz inclusions in both meta-igneous rocks show the same oxygen isotopic composition as the quartz in the matrix (13.6-13.9‰). In whiteschist the oxygen isotope composition of quartz included in tourmaline cores lost their igneous signature, having the same values as quartz in the matrix (11.4-11.7‰). A network of small fractures filled with dravitic tourmaline can be observed in the igneous core and suggested to serve as connection between included quartz and matrix, and lead to recrystallization of the inclusion. In contrast, igneous core of the whiteschist tourmaline fully retained its magmatic oxygen isotope signature, indicating oxygen diffusion is extremely slow in tourmaline. Tourmaline included in high-

pressure chloritoid shows the characteristic dravitic overgrowth, demonstrating that chloritoid grew after the metasomatism responsible for the whiteschist formation, but continued to grow during the Alpine metamorphism. Our data on tourmaline and quartz show that tourmaline-bearing whiteschists originated from the related meta-leucogranites, which were locally altered by late magmatic hydrothermal fluids prior to Alpine high-pressure metamorphism.

Keywords: Tourmaline reference materials, SIMS, oxygen isotopes, whiteschist – tourmaline, quartz, Monte Rosa

Introduction

Whiteschists are high pressure talc and kyanite-bearing metamorphic rocks (Schreyer 1973). They became famous after the discovery of the ultra-high pressure (UHP) coesite and pyrope-bearing whiteschist of Dora Maira in the Alps by Chopin (1984), and are also found in nearby rocks of Gran Paradiso and Monte Rosa nappes. Their unusual chemistry (high Mg and Al content) is suggested to be produced by metasomatism of crustal protoliths (Franz et al. 2013). However, there are disagreements as to which protolith: a sedimentary origin (Schreyer 1977; Chopin 1981; Chopin and Monié 1984) or an igneous origin (Pawlig and Baumgartner 2001). Several hypotheses have been put forward for the nature of the metasomatic fluids as well as the timing of fluid-rock interaction responsible for whiteschist formation in the western Alps. Some authors proposed an Alpine water-rock interaction during subduction by slab derived fluids produced by serpentinite dehydration (Sharp et al. 1993; Ferrando et al. 2009). On the other hand, Pawlig and Baumgartner (2001) presented a genetic model for the Monte Rosa whiteschist in which the metagranite was altered into a sericite-chlorite-quartz assemblage during late hydrothermal alteration of the Permian granite prior to Alpine orogeny. Subsequent Alpine high-pressure metamorphism led to the mineralogy of the whiteschist.

To constrain the igneous, hydrothermal, and metamorphic history of the Monte Rosa whiteschist, we use oxygen isotope analyses of zoned tourmaline crystals and their quartz inclusions. Tourmaline is a common accessory mineral in the Monte Rosa granite and a minor constituent of leucogranites and aplitic dikes. It is also present locally in the whiteschist. Tourmaline is known to retain its chemical and isotopic compositions through different growth stages in changing environments, due to its very slow volume diffusion (e.g. Henry and Dutrow 1996; van Hinsberg et al. 2011a). Oxygen isotopes are excellent tracers of fluid-rock interaction (e.g. Baumgartner and Valley 2001). They can also be used for estimating temperature conditions, e.g. when applied to quartz in conjunction with a refractory accessory mineral (RAM-thermometry; see Valley 2001) like with alumosilicate (Putlitz et al. 2002), garnet (Quinn et al. 2016) or with tourmaline (Matthews et al. 2003).

Oxygen isotopes were measured in-situ by secondary ion mass spectrometry (SIMS) in order to explore quartz inclusions and distinct growth zones in tourmaline. A new set of reference materials for in-situ SIMS analysis in tourmaline has been calibrated. The development procedure of reference materials is described in detail in the first part of the study, and in the second part an application is presented. Here, oxygen isotopes data of tourmaline and quartz, combined with major element compositions on samples of metagranite, meta-leucogranite and whiteschist from the Monte Rosa nappe allow characterization of different growth events of tourmaline and provide information on the formation of the whiteschist.

Geological setting

The Monte Rosa nappe is a middle Penninic tectonic unit of the Western Alps (Fig. 1a). It belongs to the internal crystalline massifs, together with Gran Paradiso and Dora Maira. These

units are attributed to the Briançonnais microcontinent and represent the southernmost pieces of the European continental crust involved in the Alpine orogeny (Steck et al. 2015).

The Monte Rosa nappe consists of Variscan and older, polymetamorphic paragneisses (Bearth 1952). It was intruded by granitic to granodioritic rocks dated by U-Pb SHRIMP on zircons at 270 ± 4 Ma (Pawlig 2001). The intrusions consist mainly of porphyritic biotite granite with some leucogranitic bodies, crosscut by numerous aplite and pegmatite dikes (Fig. 1c). The granite locally contains 10 to 50 meter-sized bodies of whiteschist (Bearth 1952).

In this paper we focus on the whiteschist occurrence described by Pawlig and Baumgartner (2001), in the Mezzalama area, upper Ayas Valley, northern Italy. Here, Alpine metamorphism is heterogeneously recorded and tightly related to the deformation intensity (Steck et al. 2015). In low strain domains, the Alpine high-pressure parageneses are preserved in metagranite and whiteschist, whereas in high strain domains they are partially to completely overprinted by greenschist facies assemblages. A sample of metagranite was collected from an undeformed region and a meta-leucogranite from a slightly deformed region of the intrusion, north of the Mezzalama refugio. The studied whiteschist outcrop is located at the base of the Piccolo Ghiacciaio di Verra, within a weakly deformed metagranite (Fig. 1b). Here, the whiteschist is approximately 10 to 20 meters wide. Its western limit with the metagranite is cut by a SW dipping, sinistral shear zone. Shearing imposed a strong greenschist-facies foliation on the western edge of the whiteschists and in adjacent paragneisses (Pawlig and Baumgartner, 2001). The whiteschist texture is characterized by dark porphyroblasts of chloritoid in a beige-greyish matrix of talc, white mica, quartz and chlorite (Fig. 1d).

Methodology

Major element analysis by electron microprobe (EMP)

Major element analyses of tourmalines from Monte Rosa and those used as reference materials were obtained by electron microprobe using a JEOL JXA-8350F at the University of Lausanne. The instrument is equipped with a Schottky field emission gun and with five wavelength-dispersive X-ray spectrometers. The operating conditions were 15 kV acceleration voltage at 15 nA beam current with a beam size of 5 μm or 1 μm, depending on the width of the zone to analyze. Reference tourmaline grains were also analyzed using a JEOL JXA-8230 at Louisiana State University, USA. Analyses were performed at 15 kV and 20 nA, with a 5 μm spot size using well-characterized mineral standards and a tourmaline as secondary standard. Counting times on peak and on background, detection limits as well as standards used for each element are listed in the supplementary data (Tab. S1).

Six to eight grains of each tourmaline reference material were analyzed, with 10 to 25 measurements per grain, to evaluate their homogeneity.

Mineral formula of tourmaline was calculated as suggested by Henry et al. (2011), based on fixed number of cations (15) for Y + Z + T sites. Because neither Li nor B were analyzed, Li was estimated from an average of mineral formula normalization based on Si = 6 and the formula of Pesquera et al. (2016). Boron was calculated by iteration resulting in 3 atoms of B per formula unit (pfu). Hydrogen was obtained by charge balance.

To visualize chemical variations of the tourmalines from Monte Rosa samples, chemical maps of Al, Si, Fe, Mg and Na were acquired at 15 kV acceleration voltage and 50 nA beam using dwell times of 60-100 ms with the FEG-EMPA at the University of Lausanne. Same minerals served as standards as were used for quantitative major element analysis (Tab. S1).

Oxygen isotope analysis by laser heating fluorination (LF)

Oxygen isotope compositions of tourmaline reference materials were determined at the stable isotope laboratory of the University of Lausanne using a CO_2-laser fluorination technique. The analyses followed the method initially described by Sharp (1990); for the detailed procedure see Lacroix and Vennemann (2015).

During each analytical session, tourmaline aliquots of 1.5-2.3 mg were measured together with the NBS-28 quartz reference material (accepted value 9.64‰, Coplen et al. (1983)). Tourmaline data were corrected to the session value of the NBS-28 quartz and given in conventional δ-notation, relative to Vienna Standard Mean Ocean Water (VSMOW). The daily uncertainty of NBS-28 quartz was typically better than ± 0.12‰ (1SD = standard deviation). The measurement repeatability over six analytical sessions (January to November 2017) was 0.06‰ (1SD) with a measurement bias of 0.04‰ (1SD).

Secondary ion mass spectrometry (SIMS)

The Cameca IMS 1280HR secondary ion mass spectrometer (SIMS) at the SwissSIMS facility (University of Lausanne) was used to investigate the homogeneity of the oxygen isotope composition of the tourmaline reference materials. Two to seven randomly chosen grains of each tourmaline sample were analyzed by placing six to twelve points per grain. The instrumental mass fractionation (IMF) was determined for the Fe-Mg and Li tourmaline compositions common in metamorphic and igneous rocks. SIMS was also used to obtain in-situ analyses of oxygen isotope ratios of tourmaline and quartz in samples from the Monte Rosa metagranite, meta-leucogranite and whiteschist.

A Cesium-source was used to produce positive ions and to generate a primary high-density Gaussian beam of 1.5-2 nA. The beam was accelerated through a potential of 10 kV and focused on the sample to a diameter of about 10 μm. Secondary ions were extracted from the

sample and accelerated as O^- ions through a potential of -10 kV into a mass spectrometer. An electron gun compensated the surface charge of the sample. Both ^{16}O and ^{18}O were measured simultaneously by Faraday cup detectors at intensities of 1.0 - 2.0 × 10^9 cps (counts per second) and of 2.0 - 3.5 × 10^6 cps, respectively. A calibration of the mass, the Faraday cups and of the background was performed at the beginning of each session. No effects on the reproducibility of the reference materials were found between sessions with or without raster. The measurements followed the analytical protocol given by Kita et al. (2009).

The time for a single analysis was about 3.5 min, including a pre-sputtering (45 sec, to remove gold coating and potential surface impurities), an automated centering of the secondary beam in contrast and field apertures (60 sec), and an acquisition time of 100 seconds (20 cycles of 5 sec). The within-spot reproducibility (2SE = 2 × standard error) was generally between 0.15‰ and 0.25‰.

The in-situ oxygen isotope analyses of tourmaline required development of new reference materials. Detailed description of development procedure for the new set of tourmaline reference materials is given below.

The compositions of the Monte Rosa tourmalines lie on a solid-solution join between schorl and dravite. Therefore, reference materials for each analytical session included a schorl, IAEA-B-4, and a dravite, UNIL-T2. Reference material for quartz was UNIL-Q1 (Seitz et al. 2016) . All three standards also served to monitor the instrument stability and to perform drift corrections, when necessary. During all sessions the reproducibility (2SD = 2 x standard deviation of the mean of all analyses within a session) of each of the three reference materials was better than 0.27‰, after applying a linear drift correction.

Development of tourmaline reference material for in-situ oxygen isotope analysis

Here we present the first set of tourmaline reference materials for in-situ oxygen isotope ratio determination in tourmaline. Initially 16 natural tourmalines were selected to determine their usability for reference materials. Tourmalines fulfilling the following criteria were retained for a detailed study: (1) the material was homogeneous in major element composition; (2) the samples cover the chemical range of most common tourmaline compositions; (3) and a minimum amount of about 1 gram of material was available. Ideally, major element compositions close to end-members, as well as intermediate solid solutions, are required to establish the IMF. Of the 16 tested samples, seven tourmaline samples were homogeneous in chemical and oxygen isotope compositions. These tourmalines are presented here as suitable tourmaline reference material for in-situ oxygen isotope measurements by SIMS.

Sample preparation

The tourmaline samples IAEA-B-4, UNIL-T1, UNIL-T4, UNIL-T5 were obtained as crushed material. The samples UNIL-T2, UNIL-T3 and UNIL-T6 were received as single crystals. The latter were optically screened for zonations and different zones were carefully separated using a wire saw. Afterwards, the separates were crushed into small pieces. Crushed grains were sieved into several size fractions. The fractions > 300 μm were used for in-situ analyses (EMP, SIMS) and fractions < 300 μm for LF. Grains used for LF analysis were carefully examined under binocular to exclude grains containing inclusions or intergrowth with other minerals and an aliquot of 20 to 50 grains has been prepared for each sample. The new tourmaline reference materials are available on request at the SwissSIMS facility.

For in-situ measurements two to seven grains were chosen arbitrarily and mounted in epoxy resin. Attention was paid to place the grains within 8 mm of the central part of the mount in

order to avoid possible analytical artifacts (Peres et al. 2013). After grinding to expose the grains, they were polished using diamond paste, progressively decreasing the diamond granulometry from 15 to 0.5 µm.

In addition to the grains, stripes were prepared to investigate potential, optically not visible, zoning of the crystal UNIL-T2, using a technique presented by Seitz et al. (2016). Three stripes were separated from top, middle and bottom of the crystal (perpendicular to c-axes) and one stripe covering the core to rim transect (parallel to c-axes). The stripes were polished as described previously, cut out of the epoxy and pressed in indium. All mounts were scanned with a white light interferometer to ensure that the local relief has less than 5 µm topography; essential for SIMS analyses (Kita et al. 2009).

Description and chemical classification

The reference material set includes seven tourmaline samples: UNIL-T1 to UNIL-T6, first characterized in this study as reference materials, and the IAEA-B-4, a well-established reference material for boron isotopes, certified by the International Atomic Energy Agency. A short description of the tourmaline samples, as well as information on their origin and literature references, where available, are given in Table 1.

The chemical composition of reference material was determined on randomly selected grains. Profiles, perpendicular and parallel to c-axes, were measured in sample UNIL-T2 to evaluate potential zoning. The results are given as mean values and their standard deviation (SD) in Table S2 of supplementary material. Recommended values are presented in Table 2.

The chemical variability is assessed through the standard deviation of the mean, which is typically below 0.5 wt.% for major elements and below 0.1 wt.% for minor elements. A slight zonation in Al and Fe is observed for UNIL-T1 schorl (0.73 wt.% and 0.82 wt.%, respectively).

220 The analytical results from two laboratories (University of Lausanne and Louisiana State
221 University) are in good agreement (Tab. S2). For the majority of elements, the differences are
222 less than 1 wt.%.
223 Tourmaline classification schemes are based on the occupancy of the different crystallographic
224 sites in the generalized structural formulae $XY_3Z_6(T_6O_{18})(BO_3)_3V_3W$ (e.g. Henry et al. 2011).
225 The X-site is filled by Na^+, Ca^{2+} or vacancies, but may also have negligible K^+. The Y-site is
226 occupied by mono-, di-, tri- or tetravalent cations, i.e. Li^+, Mg^{2+}, Fe^{2+}, Al^{3+}, Ti^{4+}. The Z-site is
227 mostly filled by Al^{3+}, but can also contain Fe^{3+}, Mg^{2+}, Cr^{3+} or V^{3+}. The tetrahedral site (T) is
228 occupied primarily by Si^{4+}, with deficiencies made up by Al^{3+}. B^{3+} is exclusively allocated to
229 the B-site. The V and W sites are occupied by anions: V-site is dominated by OH^- and
230 subordinately by O_2, W-site contains F, OH^- and O_2.
231 The reference material set includes alkali-group tourmalines with Na^+ as the dominant X-site
232 cation (Fig. 2a; Table 2). Based on the W-site anions (secondary classification), the reference
233 materials are comprised of four hydroxy-, two oxy- and one fluor-species (Fig. 2b; Table 2).
234 The available reference material set has compositions on the schorl/foitite-dravite solid solution
235 and contains also three Al-Li-dominated tourmalines (Fig. 2c; Table 2). These tourmalines
236 cover the typical compositional range of tourmalines from most granitic rocks as well as
237 metamorphic rocks (Fig. 2c). The reference materials IAEA-B-4, UNIL-T1 and UNIL-T3 are
238 chemically close to foitite (Fig. 2d). However, because Na fills more than half of their X-site
239 (Table 2), they are classified as alkali-group tourmalines and with Fe dominant as schorl and
240 not as foitite. Tourmaline UNIL-T2 is close in composition to the end-member dravite (Fig.
241 2d). The tourmalines UNIL-T4 and UNIL-T5 were described by Tonarini et al. (1998) as
242 elbaites, but according to the updated nomenclature, they are darrellhenryites. This new Li-

bearing tourmaline species was described by Novák et al. (2013) and approved by the International Mineralogical Association's Commission on New Minerals, Nomenclature and Classification in 2012. It is closely related to elbaite, but has higher aluminum and lower lithium contents and belongs to the oxy-tourmaline series (Fig. 2c).

Oxygen isotope composition and in-situ homogeneity tests by SIMS

The oxygen isotope reference values for each tourmaline were obtained from at least four replicates using the laser fluorination technique. Each replicate comprised of 1 to 3 grains, selected randomly from a previously prepared aliquot (see 'sample preparation'). The results are presented in Table 3. The reproducibility is between 0.04 and 0.10‰ (1SD) for all tourmaline samples indicating that these tourmalines are homogeneous within 0.10‰.

The potential reference materials were evaluated for homogeneity in oxygen isotopes using SIMS. A typical analysis session was less than 12 h. Blocks of 4-to-6 spot analyses in potential tourmaline reference material followed by two analysis of a reference grain. The quartz UNIL-Q1 (Seitz et al. 2016) was used as reference to monitor instrument stability and drift. Drift was found to be mostly linear, and corrections were made accordingly. The measurement repeatability of UNIL-Q1 over an entire session was typically < 0.30‰ (2SD), after drift correction. The measurement repeatability of each reference material is listed in Table 3 as 2SD. For all tested materials the measurement repeatability on a single grain was better than 0.3‰ (2SD) and the overall repeatability (all grains of a reference material) during one session was better than 0.4‰ (2SD), with exception of IAEA-B-4 on 17 December 2016. Most likely the reason for a bad reproducibility is the position of the analyzed grains on the mount because two of the six grains of IAEA-B-4 analyzed during this session were slightly outside of the recommended 8 mm circle (Kita et al. 2009). By considering only the four grains within the

circle a measurement repeatability of 0.29‰ (2SD) was obtained. Only two grains of UNIL-T3 were measured because of the small amount of material available. Nevertheless, this tourmaline is necessary to constrain the IMF as a function of chemical composition on the schorl-dravite join as it has an intermediate composition (X_{Mg} of 0.24). UNIL-T5 and UNIL-T6 have the best external reproducibility of < 0.21‰ (2SD).

Four profiles were investigated in dravite UNIL-T2 (see 'sample preparation'). Top, middle and bottom stripes were measured during the same analytical session with a measurement reproducibility of 0.34‰ (2SD). For the core to rim profile, a reproducibility of 0.32‰ (2SD) was achieved, confirming the homogeneity of the crystal.

Instrumental mass fractionation

Any oxygen isotope ratio obtained by SIMS needs to be corrected for instrumental mass fractionation (IMF). The IMF results both from the composition and structure of the analyzed material and from the instrumental tuning and configuration (Eiler et al. 1997). The later issues are caused by transmission of secondary ions (Shimizu and Hart 1982) as well as by electronic and physical effects during ion detection (Lyon et al. 1994). These processes are sample independent and can be easily corrected with one standard. However, the sample dependent fractionation is more complex. Sputtering and ionization processes are strongly affected by mineral matrix and thus vary with changing mineral structure and composition (e.g. Schroeer et al. 1973; Williams 1979; Yu and Lang 1986). Studies have shown that IMF can vary systematically by over 10‰ (Eiler et al. 1997; Riciputi et al. 1998; Page et al. 2010; Ickert and Stern 2013; Śliwiński et al. 2016). The functional dependence of IMF on mineral composition can be linear, as in biotite (Siron et al. 2016) or more complex, as in garnets (Ickert and Stern 2013) or carbonates (Śliwiński et al. 2016).

IMF can be expressed in α-notation as the ratio of absolute value of a reference material (measured e.g. by LF) and the value determined by SIMS:

$$\alpha_{IMF} = \alpha_{LF}/\alpha_{SIMS} \quad (1)$$

This equation can be approximated for small isotopic fractionations of a few permille observed here (Rumble 1982):

$$IMF = \delta^{18}O_{SIMS} - \delta^{18}O_{LF} \quad (2)$$

where $\delta^{18}O_{SIMS}$ is the oxygen isotope ratio of a reference material obtained in a SIMS analytical session and $\delta^{18}O_{LF}$ is the corresponding reference value measured by LF.

The measurement uncertainty of the IMF considers both the measurement repeatability of SIMS analyses ($2SD_{SIMS}$ of all measurements obtained for one reference material during one analytical session) and the uncertainties on the laser fluorination analyses ($2SD_{LF}$ of the reference value composite from all corrected laser fluorination measurements for the same reference material):

$$s_{IMF} = \sqrt{(2SD_{SIMS})^2 + (2SD_{LF})^2} \quad (3)$$

To investigate how chemical composition of tourmalines influences the IMF, three analytical sessions were performed, in which all reference materials were analyzed together in a single mount. The results are summarized in Table 4. IMF as a function of composition varies for these tourmalines between 1.8‰ and 2.7‰, depending on the individual analytical session.

A priori it is not clear which elements will influence the IMF; hence several different elements and selected combinations were tested to describe the observed IMF using a weighted least-square fit. The selected procedures were guided by the criteria of simplicity and ease of use. The combination of Fe and Al, given in atoms per formula unit (apfu), provided the most satisfactory IMF correction procedure for the compositional space investigated here. A typical

fit is shown in Figure 3a, where measured IMF is plotted against calculated IMF for each reference material using Fe and Al as parameters. The quality of the fit is given by the reduced χ^2 per point and is 1.050.

The variation of IMF with the composition is shown in Figure 3b. A linear correlation is present between IMF and Fe on the schorl-dravite solid solution and between IMF and Al from schorl or dravite towards Al-rich compositions. IMF decreases by about 2‰ with decreasing Fe content, more precisely from schorl to dravite. This Mg-Fe exchange related IMF is also known from other minerals forming Mg-Fe solid solutions, for example for olivine and Ca-poor pyroxenes (Valley and Kita 2009) as well as for biotite (Siron et al. 2016). A slight decrease of IMF (< 0.6‰) with increasing Al content can be observed on the schorl-elbaite-darrellhenryite solid solution. In contrast, IMF increases with increasing Al content by about 2‰ along dravite-elbaite-darrellhenryite line, however this solid solution is not continuous.

It is important to note, that the absolute IMF values change for different sessions. This is due to small changes in analytical conditions (e.g. primary current intensity, pressure of the analytical chamber). Therefore, for every analytical session, we recommend the use of bracketing tourmaline compositions, e.g. to use IAEA-B-4 or UNIL-T1 (schorl end-member) and UNIL-T2 (dravite end-member) as reference material while analyzing tourmaline of chemical composition lying between schorl/foitite and dravite. For tourmalines with more than 7 apfu Al, one of the three Al-rich reference materials should be analyzed in addition to schorl and dravite reference materials.

Application to tourmaline of the Monte Rosa nappe

Sample description and petrography

We investigated five samples from the Monte Rosa nappe: one metagranite (15MR40), one meta-leucogranite (15MR34) and three whiteschist samples (16MR36, 16MR39, 16MR44) (Fig. 1b) in order to approach the origin and chronological history of the Monte Rosa whiteschist.

Sample 15MR40 is a porphyritic undeformed **metagranite**, containing igneous K-feldspar, plagioclase, biotite and quartz (Fig. 4a). K-feldspar defines a magmatic foliation and forms crystals up to five centimeters in length. Most plagioclase has been pseudomorphosed to fine-grained zoisite, albite and white mica. However, polysynthetic twinning remains visible in some crystals. Similarly, some biotite is replaced by phengite, titanite, and minor garnet (Fig. 4b). These pseudomorphic assemblages reflect the Alpine high-pressure metamorphism (Luisier 2018). A greenschist-facies overprint is recorded by chlorite, which locally replaces relict biotite, and albite-zoisite pseudomorphs are locally recrystallized into Fe-rich clinozoisite, albite and white mica. Accessory phases are tourmaline, titanite, zircon, apatite, monazite and ilmenite.

Tourmaline is rare and is mostly included in K-feldspar. The grains are smaller than one millimeter in size (Figs. 4a - 4c) and form idiomorphic to hypidiomorphic crystals with orange-brown cores and a thin dark blue rim (Fig. 4c). Typically, the core shows a patchy zonation. Oscillatory zoning of the core, observed as green-to-orange color zoning, is less common and present only in crystals > 250 µm. The thickness of the rim varies from 2 to 70 µm, depending on which crystal faces the overgrowth was formed (Fig. 4c).

Sample 15MR34 is a coarse-grained, weakly deformed **meta-leucogranite** containing igneous K-feldspar (mostly microcline), plagioclase, white mica, quartz, tourmaline and garnet (Fig. 4d). K-feldspar forms centimeter-size crystals while other minerals are plurimillimetric.

Plagioclase is partially pseudomorphosed by a fine-grained sericite, albite and clinozoisite assemblage. Quartz shows recrystallization textures, such as irregular grain boundaries and sub-grain domains. Accessory phases are rutile, ilmenite, apatite and zircon. The volume portion of tourmaline in this sample is about 5%. Tourmaline has well developed idiomorphic to hypidiomorphic forms. The crystals display a bright greenish euhedral inner zone and an orange-to-greenish brown outer zone surrounded by a dark-blue rim, similar to those observed in metagranite (Figs. 4d and 4e). The size of tourmaline crystals varies from a few hundred micrometers up to a few centimeters. Larger tourmaline crystals are typically fractured or even broken apart and the dark blue overgrowth develops also on fracture sites (Figs. 5d and 5e). Quartz inclusions in tourmaline are rare and usually do not exceed 20 μm.

Sample 16MR39 is a coarse-grained, undeformed **whiteschist**, made up of plurimillimetric chloritoid, talc, white mica, chlorite and quartz (Fig. 4h). A fine-grained chlorite and sericite assemblage partly replaces chloritoid. The fine-grained matrix is formed by unoriented, talc, phengite and retrograde chlorite and sericite. Tourmaline is present in the matrix and as inclusions in chloritoid.

Sample 16MR44 is a foliated **whiteschist** containing quartz, phengite, sericite and chlorite (Fig. 4g). Chlorite and sericite nearly completely replace chloritoid, forming well visible pseudomorphs. White micas and quartz define a pronounced schistosity. Elongated tourmaline crystals follow the schistosity, whereas small roundish tourmaline grains are randomly distributed.

Sample 16MR36 is a quartz-rich, fine-grained and strongly foliated **whiteschist** (Fig. 4f). It consists mainly of quartz, phengite and chloritoid. White mica is deflected around chloritoid porphyroblasts and defines the schistosity. Quartz is recrystallized forming lobate grain

boundaries. Chlorite and sericite partially replace chloritoid. Tourmaline crystals are typically associated with white mica and in some cases are following the schistosity.

In all whiteschist samples, accessory phases include apatite, allanite, monazite, zircon, rutile, and ilmenite.

Sample 16MR36 has the lowest tourmaline content (1 to 2 Vol.%), sample 16MR39 has 3 to 4 Vol.% and sample 16MR44 has the highest tourmaline content (up to 5 Vol.%). Common in all whiteschist samples is the size of tourmaline grains: 10 to 20% of all tourmaline grains are larger than 500 μm, whereas the remaining 80 to 90% are clearly smaller (< 200 μm). Tourmaline shows similar colors and zoning patterns in all whiteschist samples: A blue inner zone, a yellowish-green outer zone with oscillatory zoning, surrounded by a light yellowish-beige overgrowth (Figs. 4f - 4k). The light rim can be observed in tourmaline in the matrix as well as in tourmaline included in other minerals, such as white mica or chloritoid (Fig. 4h). The rim of tourmaline associated with white mica and talc is typically thicker (50 – 200 μm) than the rim of tourmaline within quartz-rich domains or tourmaline included in chloritoid (< 20 μm) (Figs. 4f - 4k). Tourmaline cores are xenomorphic and strongly resorbed, while the overgrowth is idiomorphic to hypidiomorphic (Fig. 4k). Tourmaline cores are commonly fractured, forming a micro-crack-network. In contrast, the rims do not show signs of fracturing (Figs. 4i - 4k). Quartz inclusions, up to 200 μm in size, are mostly present in the tourmaline cores (Fig. 4j), but they are smaller (< 20 μm) and rarely observed in the rim.

Chemical composition of tourmaline

The tourmaline compositions are essentially on the binary Fe-Mg join, with slight deviations in Al (Fig. 5). In general, tourmaline cores are Al-rich and close to oxy-schorl/foitite in their compositions (dark symbols), whereas tourmaline rims are slightly depleted in Al (bright

symbols) and plot closer to schorl-dravite join. Remarkably, tourmaline cores from meta-leucogranite and from three whiteschist samples are very similar in chemical compositions and plot close to Fe-rich foitite/oxy-schorl. The core of metagranitic tourmaline is different and has an intermediate composition between oxy-schorl and oxy-dravite. Tourmaline rims are clearly distinct in chemistry from their corresponding cores. In metagranite and meta-leucogranite the tourmaline rims are, compared to the cores, depleted in Al, while the Fe-Mg ratio remains almost the same. However, the depletion in Al is more pronounced in metagranite than in meta-leucogranite. Larger differences in chemistry between core and rim are present in whiteschist samples. Here, tourmaline cores are Fe-rich, whereas the rims are close to the dravite end-member chemistry and therefore dominated by Mg.

The X-ray maps of Mg together with major element profiles best illustrate the main differences between the samples as well as between distinct growth zones within a crystal (Fig. 6). Representative rim and core compositions of tourmalines from all studied samples are presented as supplementary data in Table S3. Metagranitic tourmaline is slightly higher in Mg compared to tourmaline cores from meta-leucogranite and whiteschist, although the whiteschist tourmalines rim, as well as small fractures within its core, reveal the highest Mg content (Fig. 6). A patchy zoned core with a homogeneous rim characterizes the tourmaline from metagranite, whereas in tourmaline cores of meta-leucogranite and whiteschist oscillatory zoning is present. This oscillatory zoning is well displayed by chemical mapping. Tourmalines of meta-leucogranite and whiteschist show similar zoning patterns within their cores: A small inner zone, in general homogeneous in composition and slightly depleted in Na; and an outer zone, typically showing small alternating variations (orders of a few μg/g) (Figs. 6b and 6c). Tourmaline rim compositions from meta-leucogranite and whiteschist are however clearly

different. Tourmaline in whiteschist develops a dravitic overgrowth on strongly resorbed cores (Figs. 4i, 5 and 6). Here, Mg increases from 0.5 apfu, and Na from 0.6 apfu in the core up to 2.8 apfu and 0.8 apfu in the rim, respectively. These changes are compensated by a decrease in Fe (by 1.5 apfu) and Al (by 0.9 apfu). In contrast, the rims of meta-leucogranitic tourmaline are characterized by a thin overgrowth on an almost idiomorphic core. Na and Fe slightly decrease from core to rim, while Mg slightly increases. Here, all chemical changes from core to rim are less than 0.25 apfu. Similarly, the tourmaline from metagranite shows small chemical changes from core to rim. Na and Ca increase by 0.2 apfu each, Fe as well as Mg by about 0.5 apfu, while Al decreases by about 0.8 apfu.

Consequently, the tourmaline cores of meta-leucogranite and whiteschist are not only similar in composition but also show similar zoning patterns. However, their rims record completely different chemistry. Tourmaline from metagranite is clearly different in its chemistry and zoning from meta-leucogranite and whiteschist tourmalines.

Oxygen isotope composition of tourmaline and quartz

The oxygen isotope compositions of tourmaline grains from each sample were investigated by in-situ SIMS analysis using the reference material presented previously. $\delta^{18}O$ values were also determined in quartz from the matrix and quartz included in tourmaline. Profiles were obtained from each tourmaline grain and several quartz grains in order to evaluate potential zonations.

The oxygen isotope ratios of quartz are in the range of 11.0‰ to 14.3‰, while tourmaline varies between 8.6‰ and 11.9‰ (Fig. 7). Quartz defines a narrow range of 0.9‰ within each sample, but distinct differences are observed between the rock types. Values of 13.1-14.0‰ and 13.4-14.3‰ were obtained from metagranite and meta-leucogranite, respectively. However, in the whiteschists, quartz has lower $\delta^{18}O$ values, covering the range of 11.0‰ to 12.2‰. The

quartz-rich whiteschist samples (16MR36 and 16MR44) yield similar ranges for quartz (11.3-11.9‰ and 11.3-12.2‰, respectively). The quartz-poor sample 16MR39 has slightly lower $\delta^{18}O$ values (11.0-11.9‰).

In Figure 7, oxygen isotope ratios of tourmaline in metagranite and meta-leucogranite show narrow ranges (10.4-11.3‰ and 11.0-11.9‰, respectively), with slightly lower values in metagranite. Within the whiteschists, tourmaline yield two distinct $\delta^{18}O$ compositional ranges: 10.7-11.9‰, similar to those reported from granitic and leucogranitic tourmalines, and a range of lower $\delta^{18}O$ values of 8.6-9.8‰. A small shift to isotopically lighter oxygen compositions, similar to those reported for quartz-poor sample 16MR39, is also observed for tourmaline.

The spatial distribution of measured $\delta^{18}O$ values is shown in Figure 8. No zonation in oxygen isotopes for individual quartz grains was observed in any sample. Similar values were obtained for quartz inclusions from tourmaline core and rim (Fig. 8c). Within all samples, $\delta^{18}O$ values obtained from quartz included in tourmaline and quartz in the matrix are similar (Figs. 8a; 8c; 8d).

Despite the variations in major elements in the tourmaline cores, there is no zonation in oxygen isotopes (Fig. 8). Furthermore, the rim and core $\delta^{18}O$ values of metagranitic and meta-leucogranitic tourmaline are the same (Figs. 8a and 8b). In whiteschist, the differences between core and rim are not only reported in major elements but also in oxygen isotopes: higher values are measured in tourmaline cores, whereas dravitic tourmaline rims are up to 2‰ lower (Figs. 8c and 8d).

Discussion

Oxygen isotopes equilibrium and thermometry. Quartz-tourmaline pairs can be used to estimate temperatures (Kotzer et al. 1993; Zheng 1993; Jiang 1998; Matthews et al. 2003).

Figure 9 shows the distribution of oxygen isotopic values for quartz-tourmaline pairs from granite, leucogranite and whiteschist. The isotherms are plotted using the equation of Matthews et al. (2003). The oxygen isotope ratios of quartz-tourmaline pairs from metagranite and meta-leucogranite plot in a narrow range, suggesting tourmaline could be close to equilibrium with quartz. This contrasts with data from whiteschist; here only the tourmaline rims are close to equilibrium with the quartz (both matrix- and inclusion-quartz) whereas the tourmaline cores are not. The later preserved the igneous isotope signature, similar to values reported from metagranite and meta-leucogranite. Apparently, quartz included in tourmaline was completely recrystallized and show the same isotopic ratios as matrix quartz. It seems to have equilibrated with dravitic tourmaline present in rims and fractures. At first glance, this result is surprising, as it is to be expected that inclusion is in equilibrium with its host and is protected against metasomatic alteration or metamorphism. Nevertheless, as discussed above a fine micro-fracture-network is a typical feature of the studied tourmaline cores (Figs. 4 and 6). Elemental X-ray maps reveal the micro-cracks to be filled with tourmaline of the same composition as the rim (well visible by the red color in Figure 10). The micro-fractures build a connection between quartz inclusions and the exterior of the core. Linked to the matrix, quartz inclusions could easily recrystallize and change their oxygen isotopic composition. Apparently, tourmaline cores could not serve as a closed container to retain the igneous signature of its inclusions. In a study on oxygen isotope thermometry using quartz inclusions in garnet, Quinn et al. (2016) demonstrated that armored quartz inclusions and their garnet hosts can be used to obtain metamorphic temperatures, provided that the quartz inclusion is primary and there is no indication of fractures within the host.

The quartz-tourmaline pairs from metagranite and meta-leucogranite give a temperature range between 500°C and 600°C (Fig. 9), indicating equilibration of the two minerals clearly below the water-saturated granite solidus of 650°C (e.g. Johannes and Holtz 1996). This is a known phenomenon observed in studies on granitic rocks using oxygen isotope fractionation factors between quartz and its coexisting minerals (e.g. O'Neil et al. 1977). Numerical model for intercrystalline stable isotope diffusion (Eiler et al. 1992), confirmed by natural studies (e.g. Putlitz et al. 2002) show the importance of mineral modes and grain size distribution within the rock as well as diffusional characteristics of each constituent while evaluating temperatures obtained from mineral pairs. The small difference in $\delta^{18}O$ values of quartz between quartz-rich and quartz-poor whiteschists could reflect the modal abundances or simply slight changes in fluid-rock interaction. The present study shows that tourmaline, once formed, does not exchange with other minerals. Apparently, the exchange is slow to negligible. It is not affected by alteration or metamorphism.

Nevertheless, quartz is known to exchange to lower temperatures (e.g. Eiler et al. 1993) as there are other constituents in the granitic rock. Thus, quartz continues to exchange with other fast-diffusion minerals, like micas and feldspars, during cooling and subsequent metamorphic events. For example, Quinn et al. (2016) concluded in their study that fractionation factors between garnet and matrix quartz are inappropriate when applied to a rock containing significant amount of minerals which exchange to lower temperatures. Therefore, the low temperatures obtained in this study from tourmaline-quartz oxygen isotope thermometry in metagranite and meta-leucogranite could not be interpreted as intrusion temperatures, but are most probably reset.

In whiteschist, only the tourmaline rim is in apparent equilibrium with quartz, revealing a large temperature range between 495°C and 715°C. The higher temperatures (> 600°C) are restricted to the sample 16MR36, a quartz-rich whiteschist, whereas white mica and talc dominated samples 16MR39 and 16MR44 give temperatures below 615°C. All whiteschist samples are from the same outcrop, and hence they did not experienced different peak metamorphic temperatures. These large temperature variations are probably related to the modal abundances of coexisting minerals in the rock. As reported by Eiler et al. (1993) minerals modes play an important role during isotope fractionation and thus rocks with the same coexisting minerals, but different mineral modes may display different apparent temperatures. Finally, the calibration of the quartz-tourmaline fractionation is based on schorl-rich tourmaline compositions. Hence, it might not be appropriate for dravite-quartz fractionation. Several studies have shown that elemental substitutions can have a significant effect on isotope fractionation factors (Chacko et al. 2001). Tourmaline is a complex mineral with a number of coupled substitutions and it is very likely that there are significant differences between isotope fractionation factors for different end-members, but experimental data is lacking.

The mean of the temperature range (~ 600°C), reported here from oxygen isotope fractionation between tourmaline and quartz in whiteschist samples, are slightly higher than peak metamorphic temperature of 570°C, reported from thermodynamic calculations (Luisier 2018).

Growth stages of the tourmaline. Textural and chemical observations suggest at least two distinct growth episodes of tourmaline in the studied rocks. The first stage is recorded in the tourmaline core, which can be optically and chemically subdivided into an inner and outer zone. The rim represents the second growth episode.

539 The small inner roundish zones, mostly observed in meta-leucogranite and whiteschists,
540 represent the initial growth stage of tourmaline (Figs. 4d, 4i, 4j, 6). They are blue-greenish in
541 plane-polarized light (ppl) and show a homogeneous chemical composition with slightly higher
542 Al content when compared to the outer zone (Fig. 6b). The outer zone is optically homogeneous
543 (Figs. 4d, 4i and 4j), but elemental maps reveal fine-scale oscillatory zoning (Figs. 6 and 8).
544 The zoning patterns are sharp and euhedral, indicating either a continuous growth in a system
545 with slight changes in physical or chemical conditions (e.g. Norton and Dutrow 2001), or a
546 crystal growth linked to kinetics and driven by depletion or enrichment haloes surrounding the
547 crystal. Similar characteristics were described by London et al. (1996) for disseminated primary
548 tourmaline from granite and pegmatite. No differences in oxygen isotopes were detected
549 between inner and outer zone, or among fine zones of the outer portion of the igneous core.
550 Even though tourmaline in metagranite lacks a distinct aluminous core and oscillatory zoning is
551 scarce, the fact that they are included in magmatic minerals, such as K-feldspar and plagioclase,
552 as well as their similarity in isotopic signature with the leucogranitic tourmaline confirms their
553 igneous origin. They crystallized prior to or during intrusion and emplacement of the Monte
554 Rosa granite approximately 270 ± 4 Ma years ago (Pawlig 2001).
555 The igneous growth stage is followed by a dissolution event documented by the resorption of
556 tourmaline. The extent of resorption is small to negligible in the metagranite and meta-
557 leucogranite, whereas it is well pronounced in whiteschist. This dissolution can be attributed to
558 the chemical alteration of the granite during the fluid-rock interaction event leading to the
559 chemistry of the whiteschist. Dissolution pre-dated the precipitation of all dravite rims.
560 However, alteration did not affect all plutonic rocks of the Monte Rosa massif to the same
561 extent, but was localized in specific zones. Indeed, Pawlig and Baumgartner (2001) and more

562 recently Luisier (2018) showed that pervasive alteration by fluids occurred preferentially along
563 reaction enhanced, finger-like structures and thus affected only a small part of the granitic body.
564 Furthermore, intense fracturing is present within the tourmaline cores (Figs. 4, 6, 8 and 10).
565 Tourmalines from leucogranite and whiteschist show a well-pronounced fracture network (see
566 for example Figs. 4d, 4e, 4i, 8b, 8d and 10) which post-dates resorption of tourmaline.
567 Fracturing is almost lacking in small granitic tourmaline and only rarely present in bigger ones
568 (Figs. 4c and 8a). The reasons are probably due to the small grain size and the protection by
569 igneous minerals, like K-feldspar and plagioclase, which commonly host tourmaline as
570 inclusion. In contrast, tourmaline in meta-leucogranitic and whiteschist are rarely included in
571 other minerals. In metagranite and meta-leucogranite, the fractures are overgrown by dark
572 tourmaline of the same composition as the rim (Figs. 4c, 4d and 4e). In whiteschist, the
573 fractures are filled with the same dravitic tourmaline, which encloses the igneous core (Figs. 4i,
574 6, 8c, 8d and 10). This is clear evidence that the formation of the fracture-network took place
575 before the tourmaline rim started to growth.
576 The second growth stage of tourmaline is represented by the rim and is different in each rock
577 type. In metagranite, the thin overgrowth is characterized by a decrease in Al and vacancies,
578 accompanied by a slight increase in Mg and Fe as well as Na and Ca (Fig. 6). These changes
579 are most probably related to the breakdown of biotite (release of Mg and Fe) and plagioclase
580 (release of Na and Ca) during the prograde Alpine metamorphism. In contrast to tourmaline in
581 the metagranite, tourmaline in the meta-leucogranite shows only minor changes from core to
582 rim (< 0.2 apfu). On the X-site, Na decreases while vacancies increase and on the Y-site, Fe
583 decreases while Mg increases (Fig. 6). The lack of pronounced differences in chemistry
584 between igneous core and metamorphic rim in the meta-leucogranite is likely due to the small

585 modal abundances of sheet silicates and the absence of biotite. Metamorphic reactions are
586 mostly recorded in plagioclase by the presence of fine-grained sericite and clinozoisite. There
587 are no differences recorded in oxygen isotope ratios between the core and the rim, neither in
588 metagranite nor in meta-leucogranite. This indicates, that during Alpine metamorphism,
589 reactions occurred in a closed system and oxygen isotope composition was buffered by the
590 igneous protolith. Isotope compositions are similar since the fractionation changes only slightly
591 between the metamorphic and the igneous temperatures, which is hidden by the variation of the
592 observed data (see Fig. 9).
593 In whiteschist, the second growth stage is represented by the formation of a sizeable dravitic
594 overgrowth (Figs. 4, 5 and 6). The Fe and Al content as well as vacancies decrease from core to
595 rim, while Mg and Na almost completely fill the Y- and X-sites, respectively. It is known, that
596 in metamorphic rocks, tourmaline, compared to other minerals, prefers to incorporate Mg and
597 Na (Henry and Guidotti 1985; Grew et al. 1990, 1991; von Goerne et al. 2011; Berryman et al.
598 2016). The distinct differences in composition between tourmaline core and rim in the
599 whiteschists mirror the drastic increase of the X_{Mg} of the bulk rock. The chemistry of the
600 whiteschists requires an enrichment in Mg and a depletion, among others, in Na and Ca (Pawlig
601 and Baumgartner 2001). Part of the source for boron to subsequently grow tourmaline was
602 likely stored within this metasomatized rock in sheet silicates or clay minerals. Indeed, sericite
603 can contain up to 2000 µg/g (Harder 1970). Previous data suggest that chlorite can also contain
604 substantial boron (Henry and Dutrow 1996), although recent in-situ analyses reveal lower
605 amounts for mantle derived chlorite (McCaig et al. 2018). The boron released during the early
606 stages of sericite-to-white-mica recrystallization is suggested to have been incorporated in the
607 newly forming Mg-rich tourmaline overgrowth. During the Alpine metamorphism, sericite and

608 chlorite break down to form talc, chloritoid, and white mica, and the available boron from
609 reacting sericite and chlorite breakdown induced the overgrowths of the tourmaline. Those
610 tourmaline rims with an $X_{Mg} > 0.85$ clearly mirror the new Mg-rich composition of its host
611 environment. The changes are also recorded in the oxygen isotope composition. The values of
612 the core shift from igneous values, similar to those reported from meta-leucogranites, to lower
613 values within the rim. This is clear evidence for the presence of external fluid in the rock and
614 thus an open system.
615 **Origin of the whiteschist**. The present study unequivocally identifies the protolith of the
616 whiteschist from the Monte Rosa nappe. As the major element composition reported in the
617 tourmaline cores within the whiteschists is similar to those investigated from meta-leucogranitic
618 tourmaline grains (Figs. 5 and 6), one concludes that they are inherited from the same protolith.
619 In addition, the fine oscillatory zoning, typical for igneous tourmaline, can be observed in both
620 the whiteschist and meta-leucogranite tourmalines (Fig. 6). Further, the histograms in Figure 7
621 report the same oxygen isotope signature for tourmaline cores in all studied rock types. In
622 contrast, the chemical composition of granitic tourmaline is too different from that reported
623 from whiteschist (Figs. 5 and 6). In addition, the modal abundance of tourmalines within the
624 studied whiteschists (about 2 – 5 Vol.%) is similar to that observed in meta-leucogranite, while
625 in the metagranite tourmaline is typically present as an accessory phase. Based on the
626 arguments listed above we conclude that the tourmaline-bearing whiteschists from the Monte
627 Rosa nappe originated from the leucogranitic parts of the magmatic complex. The tourmaline-
628 poor whiteschists, in contrast, can easily be derived from the Monte Rosa granite, as proposed
629 by Pawlig and Baumgartner (2001) based on geochemistry and field arguments. Hence, the

protolith of the whiteschists are clearly hydrothermally altered rocks of the granitic Monte Rosa suite.

Due to its slow volume diffusion and resistance to alteration processes, igneous tourmaline cores within the whiteschist remained chemically unaffected by the metasomatic event responsible for the formation of a strongly altered rock – the precursor of the whiteschist. Tourmaline shows only dissolution textures as reaction to this event. However, other minerals reacted and recrystallized due to a strong bulk rock chemistry change in response to infiltration of late magmatic to hydrothermal fluids (Pawlig and Baumgartner 2001). Tourmaline adapted its composition to the new rock chemistry by forming a dravitic overgrowth.

Relative timing of dravite rim growth and acquisition of whiteschist chemistry and mineralogy. The presence of a dravitic overgrowth on the igneous tourmaline included in chloritoid is the key observation constraining the chronology of the metasomatic alteration relative to high-pressure Alpine metamorphism. An example is shown in Figure 11, where the broken and resorbed igneous tourmaline core is overgrown by a thin dravitic rim and is included in chloritoid. We suggest that tourmaline was included in chloritoid after the formation of dravitic rim. Chloritoid likely grew in the whiteschist on the prograde leading to Alpine high-pressure metamorphism, at the expense of a low-grade assemblage of chlorite, mica and quartz (Chopin and Schreyer 1983; Franz 2013). As shown in Figures 11a and 11b, chloritoid is partially replaced by a retrograde assemblage consisting of chlorite and white mica. The fact that the small fractures in chloritoid show no retrograde alteration suggests that they formed even later during retrogression. Detailed X-ray maps reveal no dravite on these fractures. In addition, dravitic rim formation around tourmaline is not geometrically linked to these late fractures.

All of these observations demonstrate that metasomatic alteration must have occurred before the onset of high-pressure metamorphism. Hence, our results support the interpretation of Pawlig and Baumgarner (2001), who suggested a late magmatic hydrothermal origin for the acquisition of the whiteschist chemistry. The presently recorded whiteschist paragenesis is the result of the high-pressure metamorphism of the previously established alteration assemblage.

Implications

A new set of tourmaline reference materials presented here allows in-situ analysis of oxygen isotope compositions with the SIMS. A wide range of tourmaline with chemical compositions of the schorl-dravite solid solution series as well as Al-rich tourmalines towards the elbaite end-member can be analyzed. The IMF is determined to be a function of Fe on the schorl-dravite solid solution and of Al from schorl or dravite towards Al-rich compositions. To properly correct oxygen isotope values of unknown samples we recommend, depending on chemical composition of unknown sample, to mount at least two reference materials bracketing the compositions of the unknowns and to analyze them regularly during the session.

Large number of studies used zoned tourmaline as a powerful tool to decipher a rock origin and history, or to monitor evolving fluids (e.g. Henry and Dutrow 1996; Dutrow and Henry 2000; Marschall and Jiang 2011; van Hinsberg et al. 2011b; Berryman et al. 2017) because tourmaline is known to be one of the most retentive minerals, present in a wide range of natural rocks. The possibility to determine oxygen isotope composition in tourmaline in-situ, by using the new reference material set, and to decipher precise information from each tourmaline zone, could expand the applicability of this mineral.

The present work provides an example of how in-situ oxygen isotope analyses in tourmaline, complemented with major element chemistry and textural observations, can help to decipher the debated origin of Monte Rosa whiteschist and give insights on relative timing of formation. The protolith of the whiteschist are the associated granitic rocks of the Monte Rosa massif, as was previously proposed by Pawlig and Baumgartner (2001). Tourmaline retained its igneous composition in the core despite intense bulk composition alteration and subsequent high-pressure Alpine metamorphism. These environmental changes are reflected by the formation of tourmaline overgrowths with a new chemical composition and isotopic signature. The ability of tourmaline to retain its chemical and boron isotopic composition throughout strongly changing conditions was already demonstrated in previous studies (e.g. Henry and Dutrow 1996; Marschall et al. 2008; Marschall and Jiang 2011; van Hinsberg et al. 2011b; Berryman et al. 2017). Here we show for the first time, that this is also the case for oxygen isotopes. These features elucidate once again the advantage of slow volume diffusion of tourmaline over fast diffusion minerals, like quartz. In this study, we also show that quartz completely changes its isotopic signature with changing conditions. Even where it is included in the igneous core of a tourmaline, through small fractures it is able to exchange and to equilibrate with the matrix.

Acknowledgments

We gratefully acknowledge funding by the Swiss National Science Foundation (grants 200020-153094 and 200020-172513 supported research by KM and 200021-165756 supporting research by CL. BD gratefully acknowledges the support of the Herbette Foundation and the Swiss National Science Foundation - International Short Visit program which facilitated her sabbatical research on tourmaline and SIMS work at University of Lausanne, and the NSF

698 EAR-1551434 which facilitated portions of this study. We thank Torsten Vennemann for
699 generous access to the stable isotope laboratory. We thank Laurent Nicod for preparation of
700 excellent thin sections. Martin Robyr assisted us with the EMP and Pierre Vonlanthen with the
701 SEM. We also thank Florence Bégué and Florent Plane for their help with the tuning of the
702 SIMS. Darrell Henry is thanked for providing input on various aspects of this project and for
703 suggesting the quartz inclusion in tourmaline study. Thoughtful and constructive reviews by
704 Horst Marschall and Simon Harley improved the manuscript and are gratefully acknowledged.

References

Baumgartner, L.P., and Valley, J.W. (2001) Stable isotope transport and contact metamorphic fluid flow. Reviews in Mineralogy and Geochemistry, 43, 415–467.

Bearth, P. (1952) Geologie und Petrographie des Monte Rosa. Beitraege zur Geologischen Karte der Schweiz Lf., 96, 1–94, (in German).

Berryman, E.J., Wunder, B., Rhede, D., Schettler, G., Franz, G. and Heinrich, W. (2016) P - T - X controls on Ca and Na distribution between Mg - Al tourmaline and fluid. Contributions to Mineralogy and Petrology, 171 : 31.

Berryman, E.J., Kutzschbach, M., Trumbull, R.B., Meixner, A., van Hinsberg, V., Kasemann, S.A., and Franz, G. (2017) Tourmaline as a petrogenetic indicator in the Pfitsch Formation, Western Tauern Window, Eastern Alps. Lithos, 284, 138–155.

Chacko, T., Cole, D.R., and Horita, J. (2001) Equilibrium Oxygen, Hydrogen and Carbon Isotope Fractionation Factors Applicable to Geologic Systems. Reviews in Mineralogy and Geochemistry, 43, 1–81.

Chopin, C. (1981) Talc-Phengite: a Widespread Assemblage in High-Grade Pelitic Blueschists of the Western Alps. Journal of Petrology, 22, 628–650.

Chopin, C. (1984) Coesite and pure pyrope in high-grade blueschists of the Western Alps: a first record and some consequences. Contributions to Mineralogy and Petrology, 86, 107–118.

Chopin, C., and Monié, P. (1984) A unique magnesiochloritoid-bearing, high-pressure assemblage from the Monte Rosa, Western Alps: petrologic and ^{40}Ar-^{39}Ar radiometric study. Contributions to Mineralogy and Petrology, 87, 388–398.

727 Chopin, C., and Schreyer, W. (1983) Magnesiocarpholite and magnesiochloritoid; Two index
728 minerals of pelitic blueschists and their preliminary phase relations in the model system
729 MgO-Al_2O_3-SiO_2-H_2O. American Journal of Science, 283-A, 72–96.

730 Coplen, T.B., Kendall, C., and Hopple, J. (1983) Comparison of stable isotope reference
731 samples. Nature, 302, 236–238.

732 Dal Piaz, G.V. (2001) Geology of the Monte Rosa massif: historical review and personal
733 comments. Schweizerische Mineralogische und Petrographische Mitteilungen, 81, 275–
734 303.

735 Dutrow, B.L., and Henry, D.J. (2000) Complexly zoned fibrous tourmaline, Cruzeiro mine,
736 Minas Gerais, Brazil: A record of evolving magmatic and hydrothermal fluids. Canadian
737 Mineralogist, 38, 131–143.

738 Eiler, J.M., Baumgartner, L.P., and Valley, J.W. (1992) Intercrystalline stable isotope
739 diffusion: a fast grain boundary model. Contributions to Mineralogy and Petrology, 112,
740 543–557.

741 Eiler, J.M., Graham, C., and Valley, J.W. (1997) SIMS analysis of oxygen isotopes: matrix
742 effects in complex minerals and glasses. Chemical Geology, 138, 221–244.

743 Eiler, J.M., Valley, J.W., and Baumgartner, L.P. (1993) A New Look at Stable-Isotope
744 Thermometry. Geochimica et Cosmochimica Acta, 57, 2571–2583.

745 Ferrando, S., Frezzotti, M.L., Petrelli, M., and Compagnoni, R. (2009) Metasomatism of
746 continental crust during subduction: the UHP whiteschists from the Southern Dora-Maira
747 Massif (Italian Western Alps). Journal of Metamorphic Geology, 27, 739–756.

748 Franz, L., Romer, R.L., and de Capitani, C. (2013) Protoliths and phase petrology of

749 whiteschists. Contributions to Mineralogy and Petrology, 166, 255–274.

750 Gonfiantini, R., Tonarini, S., Gröning, M., Adorni-Braccesi, A., Al-Ammar, A.S., Astner, M.,
751 Bächler, S., Barnes, R.M., Bassett, R.L., Cocherie, A., Deyhle, A., Dini, A., Ferrara, G.,
752 Gaillardet, J., Grimm, J., Guerrot, C., Krähenbühl, U., Layne, G., Lemarchand, D.,
753 Meixner, A., Northington, D.J., Pennisi, M., Reitznerová, E., Rodushkin, I., Sugiura, N.,
754 Surberg, R., Tonn, S., Wiedenbeck, M., Wunderli, S. Xiao, Y., and Zack, T. (2003)
755 Intercomparison of Boron Isotope and Concentration Measurements. Part II: Evaluation
756 of Results. Geostandards Newsletter, 27, 41-57.

757 Grew, E.S., Chernosky, J.V., Werding, G., Abraham, K., Marquez, N., and Hinthorne, J.R.
758 (1990) Chemistry of Kornerupine and Associated Minerals, a Wet Chemical, Ion
759 Microprobe, and X-Ray Study Emphasizing Li, Be, B and F Contents. Journal of
760 Petrology, 31, 1025–1070.

761 Grew, E.S., Pertsev, N.N., Boronikhin, V.A., Borisovskiy, S.Y., Yates, M.G., and Marquez,
762 N. (1991) Serendibite in the Tayozhnoye deposit of the Aldan Shield, eastern Siberia,
763 U.S.S.R. American Mineralogist, 76, 1061–1080.

764 Harder, H. (1970) Boron content of sediments as a tool in facies analysis. Sedimentary
765 Geology, 4, 153–175.

766 Henry, D.J., and Dutrow, B.L. (1996) Metamorphic tourmaline and its petrologic
767 applications. (L.M. Anovitz, Ed.)Reviews in Mineralogy and Geochemistry, 33, 503–
768 557.

769 Henry, D.J., and Guidotti, C.V. (1985) Tourmaline as a petrogenetic indicator mineral- An
770 example from the staurolite-grade metapelites of NW Maine. American Mineralogist, 70,
771 1–15.

772 Henry, D.J., Novák, M., Hawthorne, F.C., Ertl, A., Dutrow, B.L., Uher, P., and Pezzotta, F.
773 (2011) Nomenclature of the tourmaline-supergroup minerals. American Mineralogist, 96,
774 895–913.

775 Ickert, R.B., and Stern, R.A. (2013) Matrix Corrections and Error Analysis in High-Precision
776 SIMS 18O/16O Measurements of Ca–Mg–Fe Garnet. Geostandards and Geoanalytical
777 Research, 37, 429–448.

778 Jiang, S.-Y. (1998) Stable and radiogenic isotope studies of tourmaline: an overview. Journal
779 of the Czech Geological Society, 43, 75–90.

780 Johannes, W., and Holtz, F. (1996) Petrogenesis and Experimental Petrology of Granitic
781 Rocks, 1 p. (P.J. Wyllie, A. El Coesy, W. von Engelhardt, & T. Hahn, Eds.) Vol. 22.
782 Springer Berlin Heidelberg, Berlin, Heidelberg.

783 Kita, N.T., Ushikubo, T., Fu, B., and Valley, J.W. (2009) High precision SIMS oxygen
784 isotope analysis and the effect of sample topography. Chemical Geology, 264, 43–57.

785 Kotzer, T.G., Kyser, T.K., King, R.W., and Kerrich, R. (1993) An empirical oxygen- and
786 hydrogen-isotope geothermometer for quartz-tourmaline and tourmaline-water.
787 Geochimica et Cosmochimica Acta, 57, 3421–3426.

788 Lacroix, B., and Vennemann, T. (2015) Empirical calibration of the oxygen isotope
789 fractionation between quartz and Fe–Mg-chlorite. Geochimica et Cosmochimica Acta,
790 149, 21–31.

791 London, D., Morgan, G.B., VI, and Wolf, M.B. (1996) Boron in granitic rocks and their
792 contact aureoles. Reviews in Mineralogy and Geochemistry, 33, 299–330.

793 Luisier, C. (2018) Pressure variations in the Monte Rosa Nappe, Western Alps, 216 p. Ph.D.

794 thesis, University of Lausanne, Switzerland.

795 Lussier, A.J., Aguiar, P.M., Michaelis, V.K., Kroeker, S., and Hawthorne, F.C. (2009) The
796 occurrence of tetrahedrally coordinated Al and B in tourmaline: An 11B and 27Al MAS
797 NMR study. American Mineralogist, 94, 785–792.

798 Lussier, A.J., Hawthorne, F.C., Michaelis, V.K., Aguiar, P.M., and Kroeker, S. (2011)
799 Elbaite-liddicoatite from Black Rapids glacier, Alaska. Periodico Di Mineralogia 80, 57–
800 73.

801 Lyon, I.C., Saxton, J.M., and Turner, G. (1994) Isotopic Fractionation in Secondary
802 Ionization Mass-Spectrometry. Rapid Communications in Mass Spectrometry, 8, 837–
803 843.

804 Marschall, H.R., Altherr, R., Kalt, A., and Ludwig, T. (2008) Detrital, metamorphic and
805 metasomatic tourmaline in high-pressure metasediments from Syros (Greece): intra-grain
806 boron isotope patterns determined by secondary-ion mass spectrometry. Contributions to
807 Mineralogy and Petrology, 155, 703–717.

808 Marschall, H.R., and Jiang, S.-Y. (2011) Tourmaline Isotopes: No Element Left Behind.
809 Elements, 7, 313–319.

810 Matthews, A., Putlitz, B., Hamiel, Y., and Hervig, R.L. (2003) Volatile transport during the
811 crystallization of anatectic melts: oxygen, boron and hydrogen stable isotope study on the
812 metamorphic complex of Naxos, Greece. Geochimica et Cosmochimica Acta, 67, 3145–
813 3163.

814 McCaig, A.M., Titarenko, S.S., Savov, I.P., Cliff, R.A., Banks, D., Boyce, A., Agostini, S.
815 (2018) No significant boron in the hydrated mantle of most subducting slabs. Nature

816 Communications, 9, 1–10.

817 Norton, D.L., and Dutrow, B.L. (2001) Complex behavior of magma-hydrothermal
818 processes: role of supercritical fluid. Geochimica et Cosmochimica Acta, 65, 4009–4017.

819 Novák, M., Ertl, A., Povondra, P., Galiova, M.V., Rossman, G.R., Pristacz, H., Prem, M.,
820 Giester, G., Gadas, P., and Skoda, R. (2013) Darrellhenryite,
821 Na(LiAl2)Al6(BO3)3Si6O18(OH)3O, a new mineral from the tourmaline supergroup.
822 American Mineralogist, 98, 1886–1892.

823 O'Neil, J.R., Shaw, S.E., and Flood, R.H. (1977) Oxygen and hydrogen isotope compositions
824 as indicators of granite genesis in the New England Batholith, Australia. Contributions to
825 Mineralogy and Petrology, 62, 313–328.

826 Page, F.Z., Kita, N.T., and Valley, J.W. (2010) Ion microprobe analysis of oxygen isotopes in
827 garnets of complex chemistry. Chemical Geology, 270, 9–19.

828 Pawlig, S. (2001) Geological Evolution of the Monte Rosa: Constraints from Geochronology
829 and Geochemistry of a Talc-Kyanite-Chloritoid Shear Zone within the Monte Rosa
830 Granite (Monte Rosa Nappe, Italian Western Alps), 149 p. Ph.D. thesis, University of
831 Lausanne, Switzerland.

832 Pawlig, S., and Baumgartner, L.P. (2001) Geochemistry of a talc-kyanite-chloritoid shear
833 zone within the Monte Rosa granite, Val d'Ayas, Italy. Schweizerische Mineralogische
834 und Petrographische Mitteilungen, 81, 329–346.

835 Peres, P., Kita, N.T., Valley, J.W., Fernandes, F., and Schuhmacher, M. (2013) New sample
836 holder geometry for high precision isotope analyses. (E. Napolitani, D. Giubertoni, M.
837 Bersani, M. Anderle, & A. Licciardello, Eds.)Surface and Interface Analysis, 45, 553–

556.

Pesquera, A., Gil-Crespo, P.P., Torres-Ruiz, F., Torres-Ruiz, J., and Roda-Robles, E. (2016) A multiple regression method for estimating Li in tourmaline from electron microprobe analyses. Mineralogical Magazine, 80, 1129–1133.

Putlitz, B., Valley, J.W., Matthews, A., and Katzir, Y. (2002) Oxygen isotope thermometry of quartz–Al_2SiO_5 veins in high-grade metamorphic rocks on Naxos island (Greece). Contributions to Mineralogy and Petrology, 143, 350–359.

Quinn, R.J., Kitajima, K., Nakashima, D., Spicuzza, M.J., and Valley, J.W. (2016) Oxygen isotope thermometry using quartz inclusions in garnet. Journal of Metamorphic Geology, 35, 231–252.

Riciputi, L.R., Paterson, B.A., and Ripperdan, R.L. (1998) Measurement of light stable isotope ratios by SIMS: Matrix effects for oxygen, carbon, and sulfur isotopes in minerals. International Journal of Mass Spectrometry, 178, 81–112.

Rumble, D. (1982) Stable isotope fractionation during metamorphic devolatilization reactions. Reviews in Mineralogy and Geochemistry, 10, 327–353.

Schreyer, W. (1973) Whiteschist: A High-Pressure Rock and its Geologic Significance. The Journal of Geology, 81, 735–739.

Schreyer, W. (1977) Whiteschists: Their compositions and pressure-temperature regimes based on experimental, field, and petrographic evidence. Tectonophysics, 43, 127–144.

Schroeer, J.M., Rhodin, T.N., and Bradley, R.C. (1973) A quantum-mechanical model for the ionization and excitation of atoms during sputtering. Surface Science, 34, 571–580.

Seitz, S., Baumgartner, L.P., Bouvier, A.-S., Putlitz, B., and Vennemann, T. (2016) Quartz Reference Materials for Oxygen Isotope Analysis by SIMS. Geostandards and Geoanalytical Research, 41, 69-75.

Sharp, Z.D. (1990) A laser-based microanalytical method for the in situ determination of oxygen isotope ratios of silicates and oxides. Geochimica et Cosmochimica Acta, 54, 1353–1357.

Sharp, Z.D., Essene, E.J., and Hunziker, J.C. (1993) Stable isotope geochemistry and phase equilibria of coesite-bearing whiteschists, Dora Maira Massif, western Alps. Contributions to Mineralogy and Petrology, 114, 1–12.

Shimizu, N., and Hart, S.R. (1982) Isotope fractionation in secondary ion mass spectrometry. Journal of Applied Physics, 53, 1303–1311.

Siron, G., Baumgartner, L.P., Bouvier, A.-S., Putlitz, B., and Vennemann, T. (2016) Biotite Reference Materials for SIMS 18O/16O Measurements. Geostandards and Geoanalytical Research, 41, 243–253.

Steck, A., Masson, H., and Robyr, M. (2015) Tectonics of the Monte Rosa and surrounding nappes (Switzerland and Italy): Tertiary phases of subduction, thrusting and folding in the Pennine Alps. Swiss Journal of Geosciences, 108, 3–34.

Śliwiński, M.G., Kitajima, K., Kozdon, R., Spicuzza, M.J., Fournelle, J.H., Denny, A., and Valley, J.W. (2016) Secondary Ion Mass Spectrometry Bias on Isotope Ratios in Dolomite–Ankerite, Part I: δ18O Matrix Effects. Geostandards and Geoanalytical Research, 40, 157–172.

Tonarini, S., Dini, A., and Pezzotta, F. (1998) Boron isotopic composition of zoned

(schorlelbaite) tourmalines, Mt. Capanne Li-Cs pegmatites, Elba (Italy). European Journal of Mineralogy, 10, 941–951.

Tonarini, S., Pennisi, M., Adorni-Braccesi, A., Dini, A., Ferrara, G., Gonfiantini, R., Wiedenbeck, M., and Gröning, M. (2003) Intercomparison of Boron Isotope and Concentration Measurements. Part I: Selection, Preparation and Homogeneity Tests of the Intercomparison Materials. Geostandards and Geoanalytical Research 27, 21–39.

Valley, J.W. (2001) Stable Isotope Thermometry at High Temperatures. Reviews in Mineralogy and Geochemistry, 43, 365–413.

Valley, J.W., and Kita, N.T. (2009) In situ oxygen isotope geochemistry by ion microprobe. In M. Fayek, Ed., MAC Short Course: Secondary Ion Mass Spectrometry in the Earth Sciences Vol. 41, 19–63.

van Hinsberg, V., Henry, D.J., and Dutrow, B.L. (2011a) Tourmaline as a Petrologic Forensic Mineral: A Unique Recorder of Its Geologic Past. Elements, 7, 327–332.

van Hinsberg, V., Henry, D.J., and Marschall, H.R. (2011b) Tourmaline: an ideal indicator of its host environment. The Canadian Mineralogist, 49, 1–16.

von Goerne, G., Franz, G. and van Hinsberg, V.J. (2011) Experimental determination of Na-Ca distribution between tourmaline and fluid in the system CaO-Na_2O-MgO-Al_2O_3-SiO_2-B_2O_3-H_2O. The Canadian Mineralogist, 49, 137–152.

Williams, P. (1979) The sputtering process and sputtered ion emission. Surface Science, 90, 588–634.

Yu, M.L., and Lang, N.D. (1986) Mechanisms of atomic ion emission during sputtering. Nuclear Instruments and Methods in Physics Research Section B: Beam Interactions with

Materials and Atoms, 14, 403–413.

Zheng, Y.-F. (1993) Calculation of oxygen isotope fractionation in hydroxyl-bearing silicates. Earth and Planetary Science Letters, 120, 247–263.

Figure captions

Figure 1. (a) Location map placing the Monte Rosa nappe within the Western Alps framework (modified after Dal Piaz (2001) and Steck et al., (2015)). **(b)** Sketch of the whiteschist outcrop, illustrating the relationship between metagranitie and whiteschist. A late greenschist facies shear zone overprinted the whiteschist (see Pawlig and Baumgartner (2001)). Red stars present the location of whiteschist samples in the outcrop. **(c)** Meta-leucogranitic dikes crosscut porphyritic K-feldspar metagranite; both contain tourmaline. **(d)** Whiteschist, with dark chloritoid crystals in a matrix of talc, white mica and quartz.

Figure 2. The chemistry of tourmaline reference materials plotted in tourmaline classification diagrams of Henry et al. (2011) and Henry and Guidotti (1985). (**a**) Ternary system for the primary tourmaline group classification based on X-site occupancy. All reference tourmalines belong to the alkali-group. (**b**) Ternary system for general tourmaline series classification based on W-site occupancy. The reference material set contains two oxy-, four hydroxy- and one fluor tourmaline. (**c**) Ternary diagram for Li- and Mn-bearing tourmaline species based on Y-site occupancy, assuming X-site is Na+K dominant and Z-site is fully occupied by Al. Note that Al-rich tourmalines are two darellhenryites and one elbaite. (**d**) Ternary system for tourmaline species classification based on Y+Z-site occupancy. The chemical range of

reference materials covers most important metamorphic and igneous tourmaline compositions, e.g. schorl–dravite–elbaite. Black squares represent end-member compositions.

Figure 3. (a) The instrumental mass fractionation (IMF) is a linear function of Fe (apfu) and Al_{tot} (apfu). This is illustrated in the excellent correlation in measured versus calculated IMF obtained for an individual SIMS session (see text for further explanations). **(b)** Illustration of the variation of IMF with chemical parameters: Fe (apfu) (solid solution dravite-schorl) and Al_{tot} (apfu) (solid solution schorl-elbaite-darrellhenryite). Note that the effect on IMF of Fe-Mg exchange is larger than the Al_1Li_1-Fe_2 exchange. Error bars are uncertainties of the IMF (s_{IMF}) determined as described in the text. Black squares represent end-member compositions.

Figure 4: Photomicrographs in plane-polarized light (ppl) showing representative textures of studied samples. **(a) - (c)** Metagranite (15MR40). **(a)** Tourmaline occurs as small crystals included in K-feldspar. Igneous plagioclase is mostly replaced by zoisite, albite and white mica. **(b)** The high-pressure assemblage of phengite, titanite and garnet completely or partially replaced igneous biotite. **(c)** Tourmaline within the metagranite displays an orange-brownish core with a darker grey-blue overgrowth (viewed parallel to the c-axes); the tourmaline in the upper left corner illustrates a cut nearly perpendicular to the c-axes. A quartz inclusions and thin overgrowths can be observed. **(d) - (e)** Meta-leucogranite (15MR34). **(d)** Typical assemblage in the meta-leucogranite sample contains large tourmaline crystals, which are part of K-feldspar, plagioclase, white mica, and quartz matrix. Rare igneous garnet is present. The igneous tourmaline core displays a rounded, lighter blue-green inner zone and a greenish outer zone. Note the tiny fractures fragmenting the tourmaline. **(e)** Tourmaline cut parallel to c-axes, displays igneous green-brownish zones (see Fig. 4d). A small, distinct dark-blue overgrowth covers the outside and the fracture walls of the

951 tourmaline. **(f) – (k)** Whiteschists. **(f)** The deformed whiteschist sample 16MR36 is composed
952 mainly of quartz, white mica and chloritoid. The greenschist facies assemblage, chlorite and
953 white mica, partially replace chloritoid and is associated with deformation. Dashed lines
954 represent the foliation. Zoned tourmaline grains are present in the matrix. **(g)** Chlorite and
955 sericite nearly completely replace chloritoid in the quartz-rich, deformed whiteschist sample
956 16MR44, suggesting that the deformation occurred during greenschist facies overprint. **(h)**
957 The whiteschist sample 16MR39 shows only minor retrogression. A matrix of talc, white
958 mica, chlorite, sericite and quartz contains large grains of chloritoid. Tourmaline is found in
959 the matrix and as inclusions in chloritoid. **(i)** Tourmaline from the whiteschist 16MR36
960 illustrates the typical zonation: igneous core with a light blue roundish inner core and a
961 slightly irregular and resorbed dark greenish-blue outer zone. It is overgrown by a pale beige-
962 yellowish rim. The dashed line follows the outer border of the crystal. Fractures are filled with
963 the same beige-yellowish tourmaline. **(j)** Zoned tourmaline grain with inclusions of quartz
964 (whiteschist 16MR44). Small elliptic spots are locations of SIMS analysis. **(k)** Examples of
965 greenish-blue resorbed tourmaline cores and hypidiomorphic pale beige-yellowish
966 metamorphic overgrowth. Mineral abbreviations: ab – albite, bt – biotite, chl – chlorite, cld –
967 chloritoid, czo – clinozoisite, grt – garnet, kfs – K-feldspar, ph – phengite, pl – plagioclase, qz
968 – quartz, ser – sericite, tlc – talc, ttn – titanite, tur – tourmaline, wm – white mica, zo – zoisite.
969
970
971 **Figure 5:** Tourmaline compositions plotted in an Al-(Fe+Mn)-Mg diagram. Cores of
972 tourmaline crystals from meta-leucogranite and whiteschist plot in the same place. Note that
973 cores and rims have distinct chemical compositions: tourmaline core (dark symbols) and
974 tourmaline rim (light symbols) for all studied samples. The compositions of the reference
975 material used for oxygen isotope analysis are shown for comparison. The diagram is modified

after Henry and Guidotti (1985): A – granitic rocks, B – metamorphic rocks, C – Fe^{3+}-rich rocks. Black squares represent end-member compositions.

Figure 6: Mg-X-ray maps and major element profiles of representative tourmalines from the three studied rock types (i.e. metagranite, meta-leucogranite and whiteschist). Note the similarity in composition and zoning of tourmaline cores from whiteschist and meta-leucogranite. Tourmaline in metagranite shows different zoning and composition. Tourmaline rims in whiteschist are dravite (red). The fractures are also filled with the same Mg-rich tourmaline.

Figure 7: Histograms of $\delta^{18}O$ values for quartz and tourmaline from metagranite, meta-leucogranite, and three whiteschists samples are plotted. The oxygen isotope composition of quartz reveals a similar, narrow range for metagranite and meta-leucogranite. The average values are 13.6‰ and 13.9‰, respectively. The average oxygen isotope composition of quartz in the whiteschist is lower at 11.5‰. The average oxygen isotope ratios of tourmalines in metagranite and meta-leucogranite define a narrow range of 11.0‰ and 11.5‰, respectively. The $\delta^{18}O$ values of whiteschist tourmaline show two distinct oxygen isotope signatures: an average of 11.3‰ for the core and 9.3‰ for the rim.

Figure 8: Locations and values of oxygen isotope SIMS analysis are plotted on backscatter electron images (BSE). White diamonds are $\delta^{18}O$ values measured on tourmaline and circles represent values for quartz. **(a)** Metagranite (15MR40): The igneous tourmaline crystal is homogenous in $\delta^{18}O$ despite chemical zonation observed (see BSE image and Figure 6a). No difference in $\delta^{18}O$ is observed between quartz in the matrix and quartz included in

1000 tourmaline. **(b)** Meta-leucogranite (15MR34): Tourmaline (core and rim) and quartz are
1001 homogeneous in their respective oxygen isotope signature. **(c)** Whiteschist (16MR39): The
1002 dravitic rim (black) has up to 2‰ lower $\delta^{18}O$ values than the igneous core. Quartz inclusions
1003 within the tourmaline core show the same oxygen isotope composition as quartz in the
1004 matrix. **(d)** The inner part of the tourmaline is homogeneous in oxygen isotopes despite
1005 visible zonations. Quartz inclusions have the same $\delta^{18}O$ values as quartz in the matrix. Note
1006 abundant fractures (arrows) within the tourmaline core, which are filled with dravite (black)
1007 of the same composition as the rim. The error of measurements is ± 0.3‰ (2SD).
1008
1009 **Figure 9:** The δ-δ plot illustrates the distribution of in-situ oxygen isotopic analyses for
1010 quartz-tourmaline pairs. The isotherms plotted are based on the equation of Matthews et al.
1011 (2003). Tourmaline-quartz pairs in metagranite and meta-leucogranite yield equilibrium
1012 temperatures of 500° to 650°C. Tourmaline rims (bright symbols) and quartz pairs in
1013 whiteschists also define a quite narrow range along the isotherms. Finally, igneous
1014 tourmaline cores (dark symbols with white dots) in whiteschist were paired with their quartz
1015 inclusions. Tourmaline maintained its igneous composition, while quartz inclusions re-
1016 equilibrated with matrix quartz.

1017 **Figure 10:** Detailed Mg-X-ray map of a whiteschist tourmaline (16MR44) reveals abundant
1018 fracturing of the old igneous tourmaline core. Fractures are filled with dravite of the same
1019 composition as the rim (red), demonstrating that the fracture network predates dravite
1020 growth. Black diamonds are oxygen isotope values obtained for tourmaline; white circles are
1021 $\delta^{18}O$ values of quartz. The network of micro-fractures connected the quartz inclusions with
1022 the matrix promoting isotopic exchange. The error of measurements is ± 0.3‰ (2SD).
1023 Mineral abbreviations are the same as in Figure 4.

Figure 11: (a) Plane-polarized light (ppl) photomicrographs and (b) line drawing showing an example of tourmaline grains included in relict chloritoid in a whiteschist. The alteration zone around chloritoid is composed of sericite and chlorite. It formed during retrogression to greenschist facies after the Alpine high-pressure event. Fine vertical lines highlight the cleavage and the sub-horizontal partings. **(c) - (d)** X-ray maps calculated using the intensity of Mg+50*Na to highlight the locations of dravite (yellow). Dravite was precipitated on the rim and on fracture walls of the igneous tourmaline. In contrast, no dravite is observed in cleavages or partings of chloritoid. These observations show that a) fracturing of tourmaline occurred prior to dravite growth; b) tourmaline included in chloritoid always has dravitic overgrowths; and c) dravite growth is not linked to the cleavage or partings of the chloritoid. Hence dravite growth started prior to inclusion in the chloritoid, hence pre-peak high-pressure. For further implications for timing of metasomatism and metamorphism see text. Mineral abbreviations are the same as in Figure 4.

Table 1. Source and description of the tourmaline reference materials

IAEA-B-4
Schorl, black prismatic crystals, 2-3 cm long, from Rosina pegmatite dyke hosted in a monzogranite, San Piero in Campo, Elba Island. A certified tourmaline reference material for boron isotopes from the International Atomic Energy Agency (IAEA). Described in Tonarini et al. (2003) and Gonfiantini et al. (2003). Provided by A. Dini as crushed grains as well as crystals.
UNIL-T1
Schorl, black to dark bluish, 2 cm long, overgrowth of an elbaite, from a cordierite- and tourmaline-bearing leucogranite, Catri, Elba Island. Described in Tonarini et al. (1998) as N2b. Provided by A. Dini as crushed grains.
UNIL-T2
Dravite, 3 x 4 cm, honey-brown, translucide euhedral zoned crystal, with a bright core (1 cm) and a darker overgrowth, containing minor rutile and quartz inclusions. Only the overgrowth was established as reference material. Origin is Nepal. Purchased from HAUSEN Mineraliengrosshandel GmbH.
UNIL-T3
Schorl, black thin prismatic crystal, 3-5 cm long, from North Pakistan. Provided by B. Dutrow as a single crystal.
UNIL-T4
Darrellhernryite, pale pink, 1.5-2 cm long, overgrown by a schorl, from a cordierite- and tourmaline-bearing leucogranite, Catri, Elba Island. Contains minor quartz inclusions. Described in Tonarini et al. (1998) as N2a elbaite. Provided by A. Dini as crushed grains.
UNIL-T5
Darrellhernryite, pale green to yellow, 2.5-3 cm long, from S.Silvestro dike hosted in monzogranite, San Piero in Campo, Elba Island. Described in Tonarini et al. (1998) as N1c/a elbaite. Provided by A. Dini as crushed grains.
UNIL-T6
Fluor-Elbaite, light pink euhedral core overgrown by green liddicoatite rim, 2 x 1.5 cm slice, from Black Rapids glacier, Alaska. Described as AT6 in Lussier et al. (2009) and Lussier et al. (2011). Provided by B. Dutrow as a 1 cm thick slice.

Table 2. Chemical composition of tourmaline reference materials (oxides in wt.%).

		IAEA-B-4	UNIL-T1	UNIL-T2	UNIL-T3	UNIL-T4	UNIL-T5	UNIL-T6
		schorl	**schorl**	**dravite**	**schorl**	**darrellhenryite**	**darrellhenryite**	**fluor-elbaite**
# grains (# analyses)		6 (n = 78)	7 (n = 87)	6 (n = 84)	8 (n = 99)	6 (n = 85)	6 (n = 84)	7 (n = 102)
B_2O_3*		10.30	10.16	10.80	10.33	11.03	10.84	10.97
SiO_2		34.61	34.04	36.46	35.07	37.38	36.77	37.59
Al_2O_3		34.86	34.56	33.73	33.53	44.78	42.55	41.99
TiO_2		0.31	0.02	0.37	0.10	*b.d.l.* [a]	0.06	*b.d.l.* [a]
FeO		13.47	14.30	0.81	12.99	*b.d.l.* [a]	0.16	0.02
MnO		0.43	0.78	*b.d.l.* [a]	0.12	0.10	3.17	0.05
MgO		0.68	*b.d.l.* [a]	10.72	2.22	*b.d.l.* [a]	*b.d.l.* [a]	*b.d.l.* [a]
Li_2O*		0.13	0.10		0.10	1.23	0.94	1.88
CaO		0.10	0.12	0.22	0.17	0.05	0.03	1.56
Na_2O		1.56	1.57	2.56	1.67	1.78	1.94	1.58
K_2O		0.03	0.02	0.08	0.02	0.01	0.01	0.01
F		0.15	0.12	0.21	0.05	0.36	0.62	0.94
H_2O*		3.30	3.38	3.58	3.48	3.21	2.96	3.23
O=F **		-0.06	-0.05	-0.09	-0.02	-0.15	-0.24	-0.39
Total		**99.89**	**99.11**	**99.45**	**99.84**	**99.77**	**99.83**	**99.43**
Normalization based on 15 Y+Z+T cations - ordered formula								
B site:	B*	3.000	3.000	3.000	3.000	3.000	3.000	3.000
T site:	Si	5.840	5.865	5.912	5.899	5.886	5.893	5.953
	Al	0.160	0.135	0.088	0.101	0.114	0.107	0.047
Z site:	Al	6.000	6.000	6.000	6.000	6.000	6.000	6.000
Y site:	Al	0.775	0.774	0.320	0.546	2.209	1.935	1.791
	Ti	0.041	0.006	0.048	0.013		0.007	
	Fe	1.906	2.100	0.105	1.798		0.021	0.003
	Mn	0.061	0.092		0.017	0.014	0.432	0.008
	Mg	0.171		2.527	0.559			
	Li*	0.045	0.028		0.067	0.777	0.604	1.197
X site:	Ca	0.019	0.021	0.038	0.031	0.009	0.006	0.265
	Na	0.511	0.520	0.797	0.545	0.543	0.604	0.485
	K	0.007	0.004	0.017	0.005	0.001	0.002	0.002
	$^{x}\square$	0.463	0.455	0.149	0.419	0.446	0.388	0.248
V site:	OH*	3.000	3.000	3.000	3.000	3.000	3.000	3.000
W-site:	OH*	0.727	0.783	0.780	0.906	0.205	0.089	0.290
	F	0.077	0.056	0.109	0.024	0.233	0.345	0.469
	O*	0.196	0.161	0.110	0.070	0.561	0.566	0.241
Al (total)		*6.934*	*6.910*	*6.408*	*6.647*	*8.323*	*8.042*	*7.839*
X_{Mg}		*0.08*	*0.00*	*0.96*	*0.24*	-	-	-

Note: *Recalculated stochiometrically according to procedures of Henry et al. (2011) (see text for details)

** correction for O=F

[a] b.d.l. - below detection limit

Table 3. Oxygen isotope reference values determined by laser fluorination (LF) and reproducibility of oxygen isotopes evaluated by secondary ion mass spectrometry (SIMS). LF: Uncertainties refer to 1 standard deviation (1SD) of the mean. SIMS: Reproducibility expressed as double standard deviations (2SD) of the mean.

	Laser fluorination (LF)			SIMS homogeneity tests			
Sample	$\delta^{18}O$ (‰)[a]	1SD (‰)	n	date	2SD (‰)	# grains	n
IAEA-B-4	11.09	0.08	6	17-Dec-16	0.45	6	36
				12-Apr-17	0.35	2	12
UNIL-T1	10.82	0.04	4	17-Dec-16	0.35	7	39
UNIL-T2	7.63	0.10	8	14-Apr-17	0.38	3	24
				21-Oct-17	0.34	3 profiles	35
				21-Oct-17	0.32	core-rim profile	29
UNIL-T3	10.37	0.08	4	14-Apr-17	0.33	2	18
UNIL-T4	11.32	0.04	4	17-Dec-16	0.37	6	33
UNIL-T5	11.29	0.05	4	17-Dec-16	0.21	4	20
UNIL-T6	12.43	0.09	4	12-Apr-17	0.21	4	48

Notes : n = number of replicates (LF) or number of spots (SIMS)

[a] Data are corrected and normalized to quartz NBS-28 (accepted $\delta^{18}O$ value is 9.64‰ relative to VSMOW)

Table 4. Results of three calibration sessions to investigate the dependence of the instrumental mass fractionation (IMF) on the chemical compositions of tourmaline.

	IAEA-B-4	UNIL-T1	UNIL-T2	UNIL-T3	UNIL-T4	UNIL-T5	UNIL-T6
16-Apr-17							
SIMS value[a] (‰)	6.61	6.36	4.18	6.08	6.32	6.50	7.93
IMF (‰)	4.48	4.46	3.45	5.24	4.05	4.79	4.50
s_{IMF}[b] (‰)	0.12	0.15	0.14	0.24	0.09	0.09	0.18
n	4	4	4	4	4	4	4
26-Nov-17							
SIMS value[a] (‰)	8.94	8.37	7.20	8.37	9.04	9.06	10.42
IMF (‰)	2.15	2.45	0.43	2.95	1.33	2.23	2.01
s_{IMF}[b] (‰)	0.13	0.08	0.11	0.11	0.10	0.12	0.13
n	14	14	9	14	14	15	11
05-March-18							
SIMS value[a] (‰)	9.80	9.27	7.95	8.94	-	9.61	11.03
IMF (‰)	1.29	1.55	-0.32	2.38	-	1.68	1.40
s_{IMF}[b] (‰)	0.10	0.12	0.16	0.15	-	0.25	0.12
n	6	3	14	3	-	3	7

Notes: n = number of measurements done during analytical session

[a]average of all measurements; [b]measurement uncertainty of the IMF, calculated as described in text

Figure 1

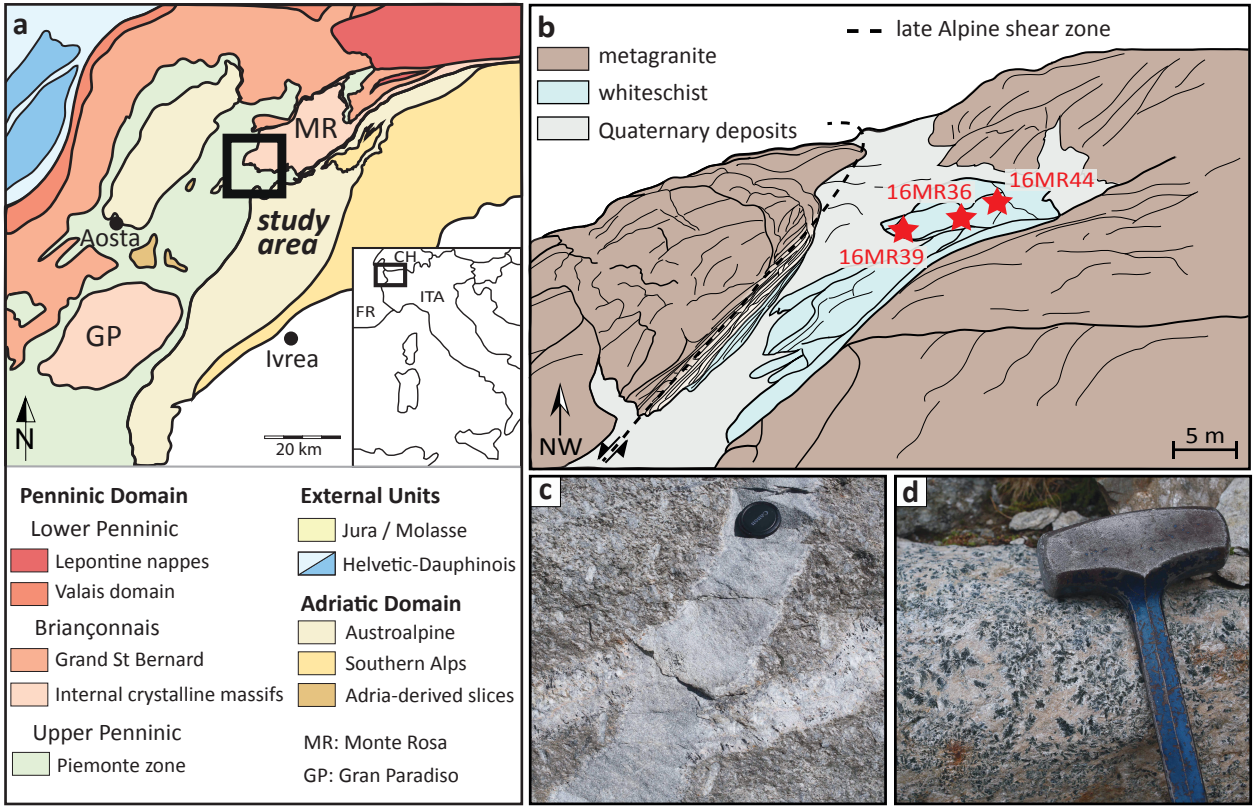
a
MR
study area
Aosta
GP
Ivrea
N
20 km
CH
ITA
FR
b
late Alpine shear zone
metagranite
whiteschist
Quaternary deposits
16MR36
16MR44
16MR39
NW
5 m
c
d
Penninic Domain
Lower Penninic
Lepontine nappes
Valais domain
Briançonnais
Grand St Bernard
Internal crystalline massifs
Upper Penninic
Piemonte zone
External Units
Jura / Molasse
Helvetic-Dauphinois
Adriatic Domain
Austroalpine
Southern Alps
Adria-derived slices
MR: Monte Rosa
GP: Gran Paradiso

Figure 2

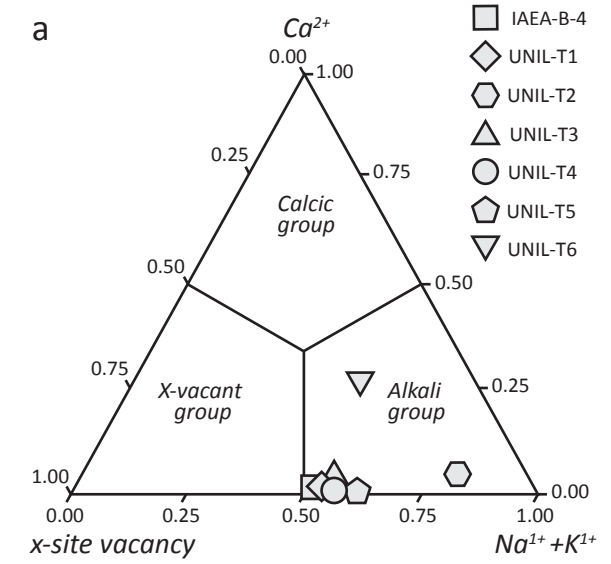
a
Ca2+
0.00
1.00
0.25
0.75
0.50
0.50
0.75
0.25
1.00
0.00
Calcic group
X-vacant group
Alkali group
x-site vacancy
Na1+ +K1+
IAEA-B-4
UNIL-T1
UNIL-T2
UNIL-T3
UNIL-T4
UNIL-T5
UNIL-T6

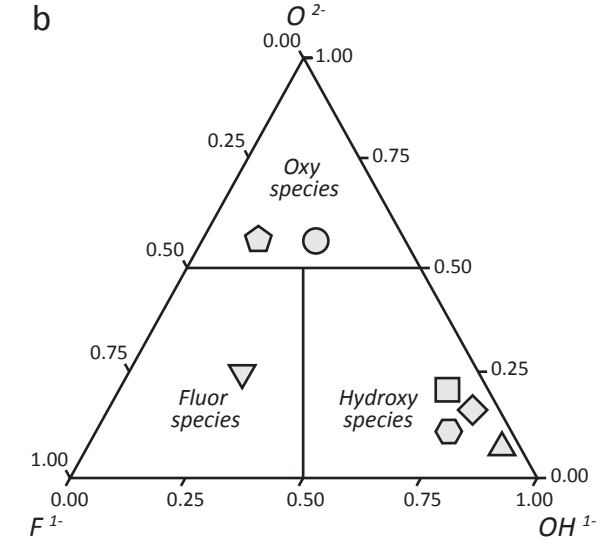
b
O 2-
Oxy species
Fluor species
Hydroxy species
F 1-
OH 1-

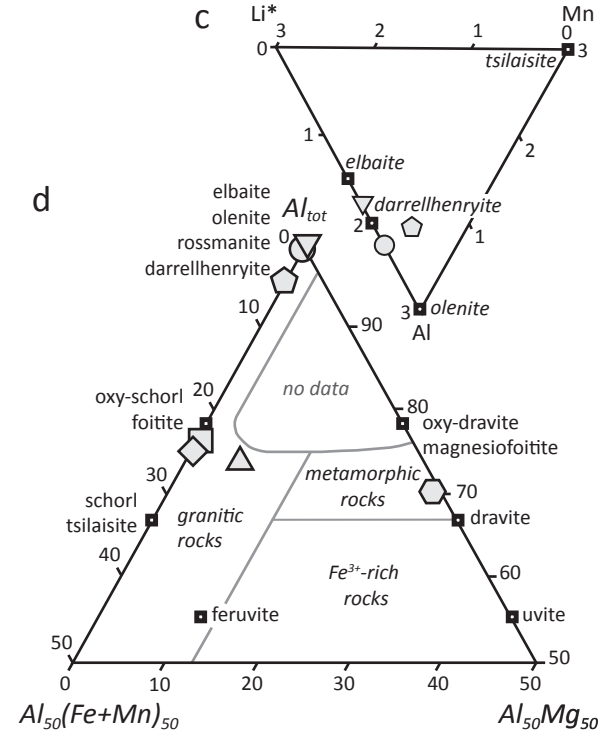
c
Li*
Mn
tsilaisite
elbaite
darrellhenryite
olenite
Al
d
Al tot
elbaite
olenite
rossmanite
darrellhenryite
oxy-schorl
foitite
schorl
tsilaisite
no data
oxy-dravite
magnesiofoitite
metamorphic rocks
granitic rocks
dravite
Fe3+-rich rocks
feruvite
uvite
Al50(Fe+Mn)50
Al50Mg50

Figure 3

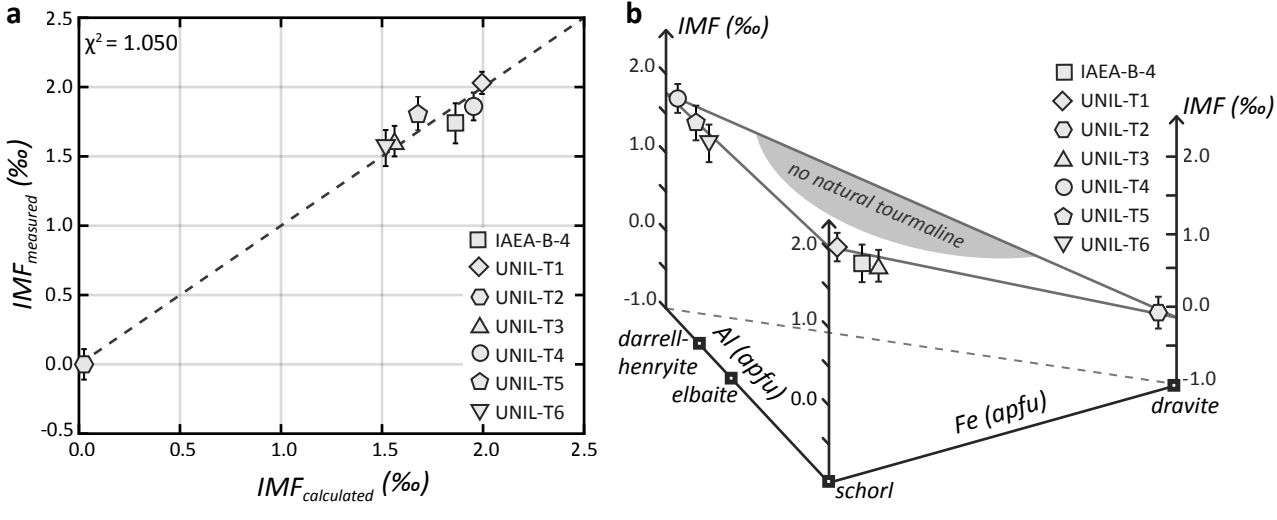
a
χ² = 1.050
IMF measured (‰)
IMF calculated (‰)
IAEA-B-4
UNIL-T1
UNIL-T2
UNIL-T3
UNIL-T4
UNIL-T5
UNIL-T6
b
IMF (‰)
no natural tourmaline
darrell-henryite
elbaite
Al (apfu)
Fe (apfu)
schorl
dravite

Figure 4

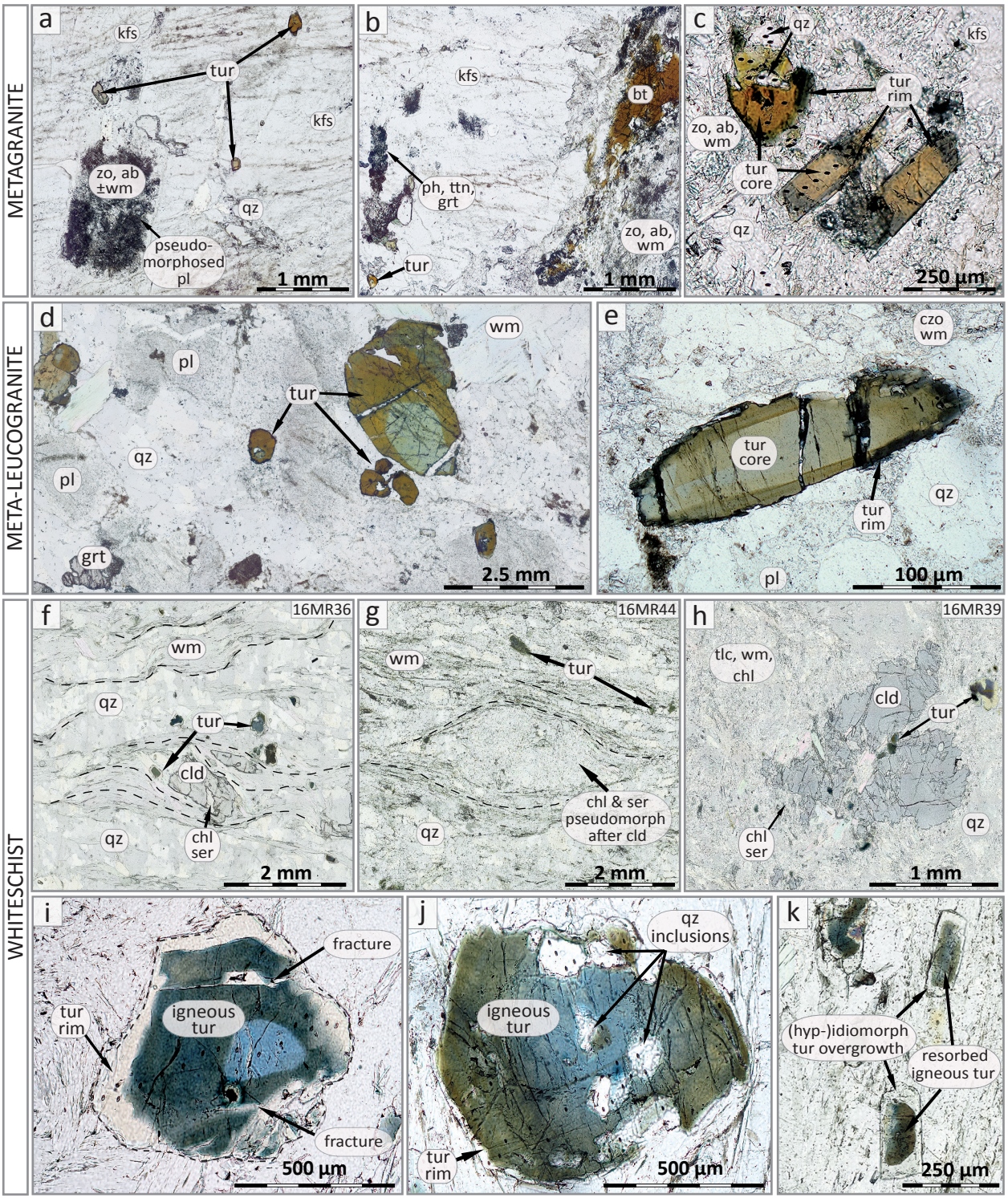
METAGRANITE
a
kfs
tur
kfs
zo, ab ±wm
qz
pseudo-morphosed pl
1 mm
b
kfs
bt
ph, ttn, grt
zo, ab, wm
tur
1 mm
c
qz
kfs
tur rim
zo, ab, wm
tur core
qz
250 µm
META-LEUCOGRANITE
d
wm
pl
tur
qz
pl
grt
2.5 mm
e
czo wm
tur core
qz
tur rim
pl
100 µm
WHITESCHIST
f
16MR36
wm
qz
tur
cld
qz
chl ser
2 mm
g
16MR44
wm
tur
chl & ser pseudomorph after cld
qz
2 mm
h
16MR39
tlc, wm, chl
cld
tur
chl ser
qz
1 mm
i
fracture
tur rim
igneous tur
fracture
500 µm
j
qz inclusions
igneous tur
tur rim
500 µm
k
(hyp-)idiomorph tur overgrowth
resorbed igneous tur
250 µm

Figure 5

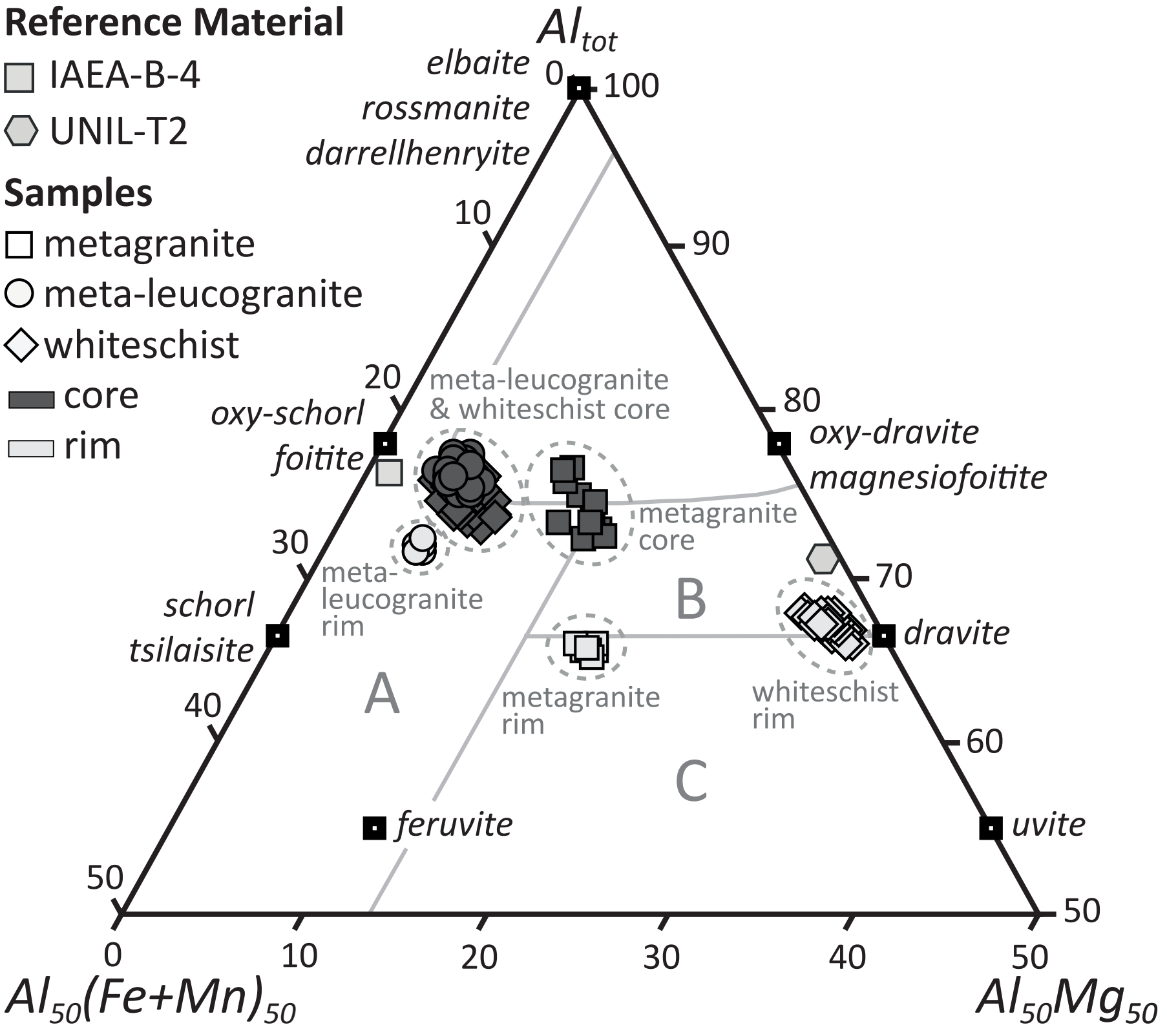
Reference Material
IAEA-B-4
UNIL-T2
Samples
metagranite
meta-leucogranite
whiteschist
core
rim
Al_{tot}
elbaite
rossmanite
darrellhenryite
0
100
10
90
20
80
30
70
40
60
50
50
oxy-schorl
foitite
schorl
tsilaisite
oxy-dravite
magnesiofoititte
dravite
uvite
feruvite
meta-leucogranite & whiteschist core
metagranite core
meta-leucogranite rim
metagranite rim
whiteschist rim
A
B
C
0
10
20
30
40
50
$Al_{50}(Fe+Mn)_{50}$
$Al_{50}Mg_{50}$

Figure 6

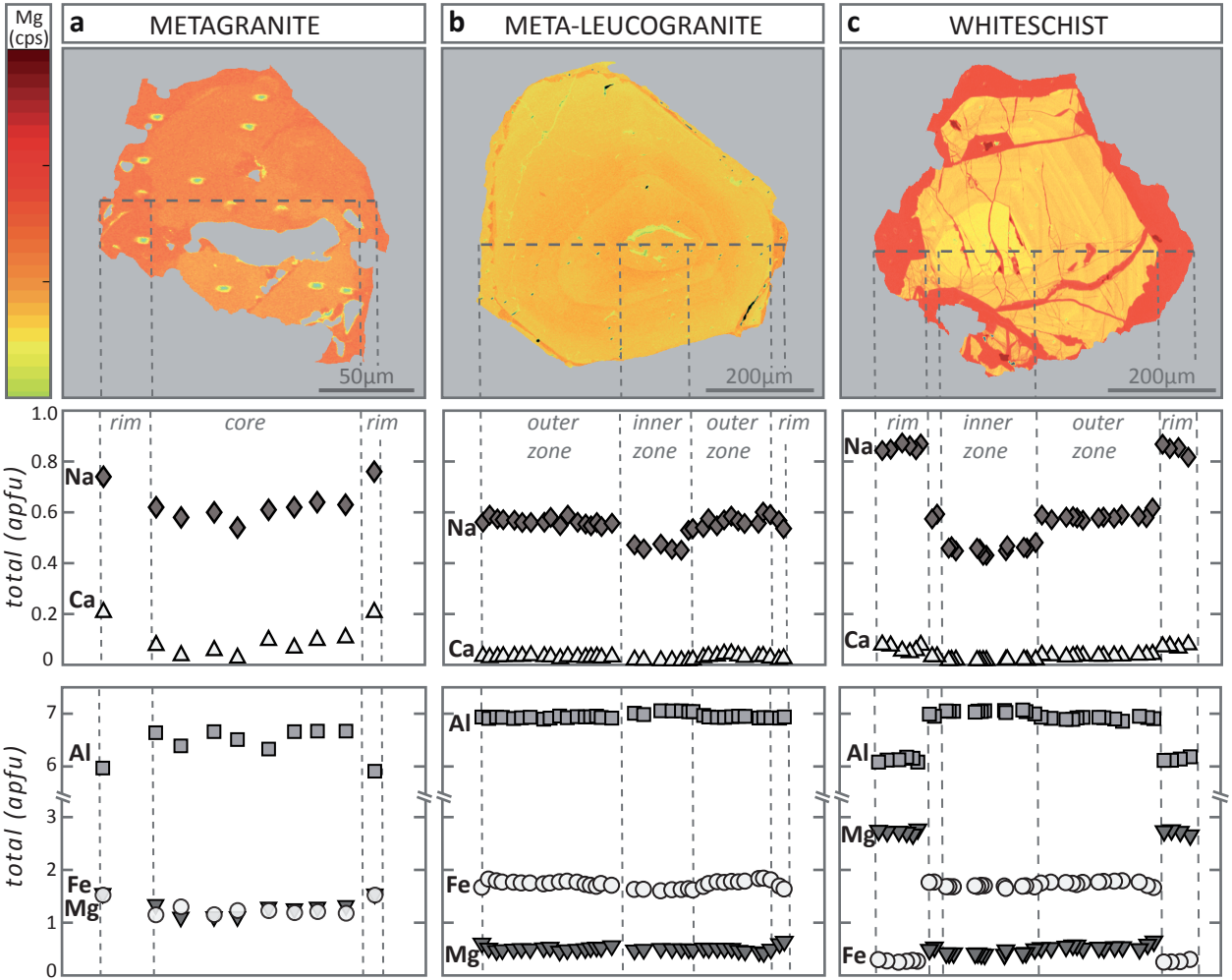
Mg (cps)
a METAGRANITE
b META-LEUCOGRANITE
c WHITESCHIST
50µm
200µm
200µm
rim
core
rim
outer zone
inner zone
outer zone
rim
rim
inner zone
outer zone
rim
total (apfu)
Na
Ca
Al
Fe
Mg
1.0
0.8
0.6
0.4
0.2
0
7
6
3
2
1
0

Figure 7

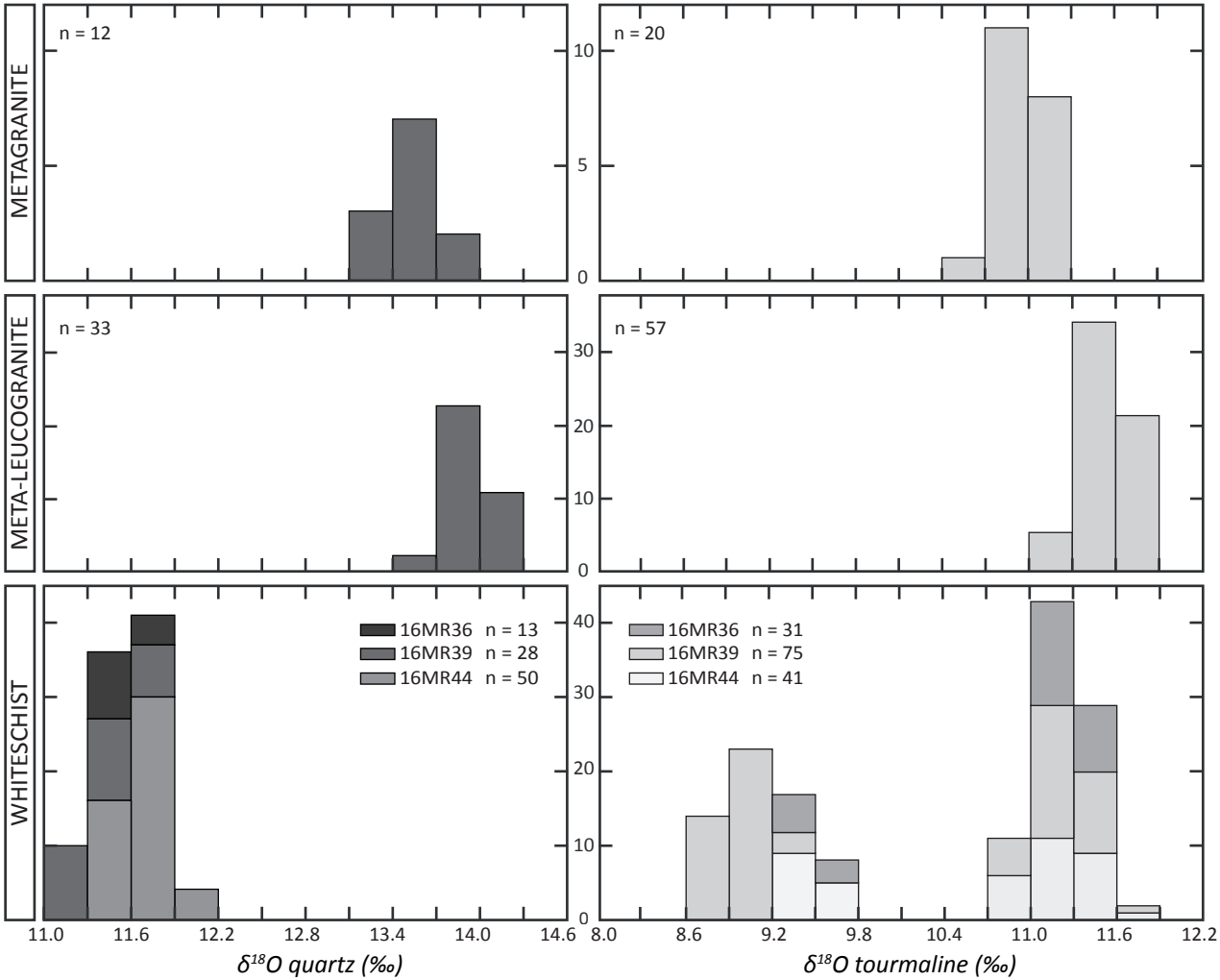
METAGRANITE
META-LEUCOGRANITE
WHITESCHIST
n = 12
n = 20
n = 33
n = 57
16MR36 n = 13
16MR39 n = 28
16MR44 n = 50
16MR36 n = 31
16MR39 n = 75
16MR44 n = 41
11.0
11.6
12.2
12.8
13.4
14.0
14.6
δ18O quartz (‰)
8.0
8.6
9.2
9.8
10.4
11.0
11.6
12.2
δ18O tourmaline (‰)

Figure 8

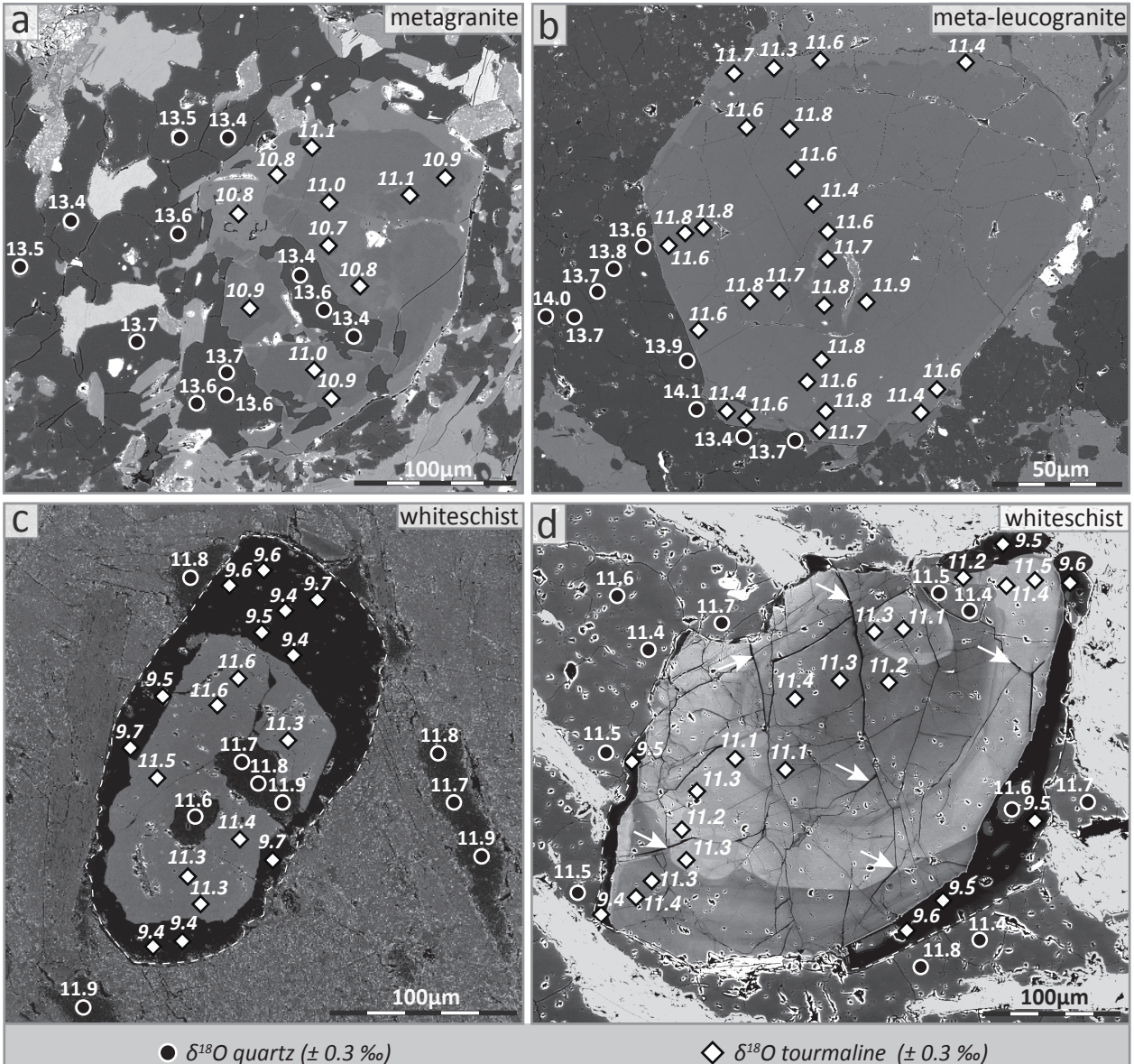
a
metagranite
13.5 13.4 11.1 10.8 10.9 13.4 10.8 11.0 11.1 13.6 10.7 13.5 13.4 10.8 10.9 13.6 13.4 13.7 11.0 13.7 10.9 13.6 13.6
100µm
b
meta-leucogranite
11.7 11.3 11.6 11.4 11.6 11.8 11.6 11.4 11.8 11.8 11.6 13.6 11.6 13.8 11.7 13.7 11.8 11.7 11.8 11.9 14.0 11.6 13.7 13.9 11.8 11.6 11.6 14.1 11.4 11.6 11.8 11.4 13.4 11.7 13.7
50µm
c
whiteschist
11.8 9.6 9.6 9.4 9.7 9.5 9.4 11.6 9.5 11.6 9.7 11.3 11.7 11.5 11.8 11.9 11.8 11.6 11.7 11.4 9.7 11.9 11.3 11.3 9.4 9.4 11.9
100µm
d
whiteschist
9.5 11.2 11.5 9.6 11.6 11.5 11.4 11.4 11.7 11.3 11.1 11.4 11.3 11.2 11.4 11.5 9.5 11.1 11.1 11.3 11.6 9.5 11.7 11.2 11.3 11.5 11.3 9.4 11.4 9.5 9.6 11.4 11.8
100µm
δ18O quartz (± 0.3 ‰)
δ18O tourmaline (± 0.3 ‰)

Figure 9

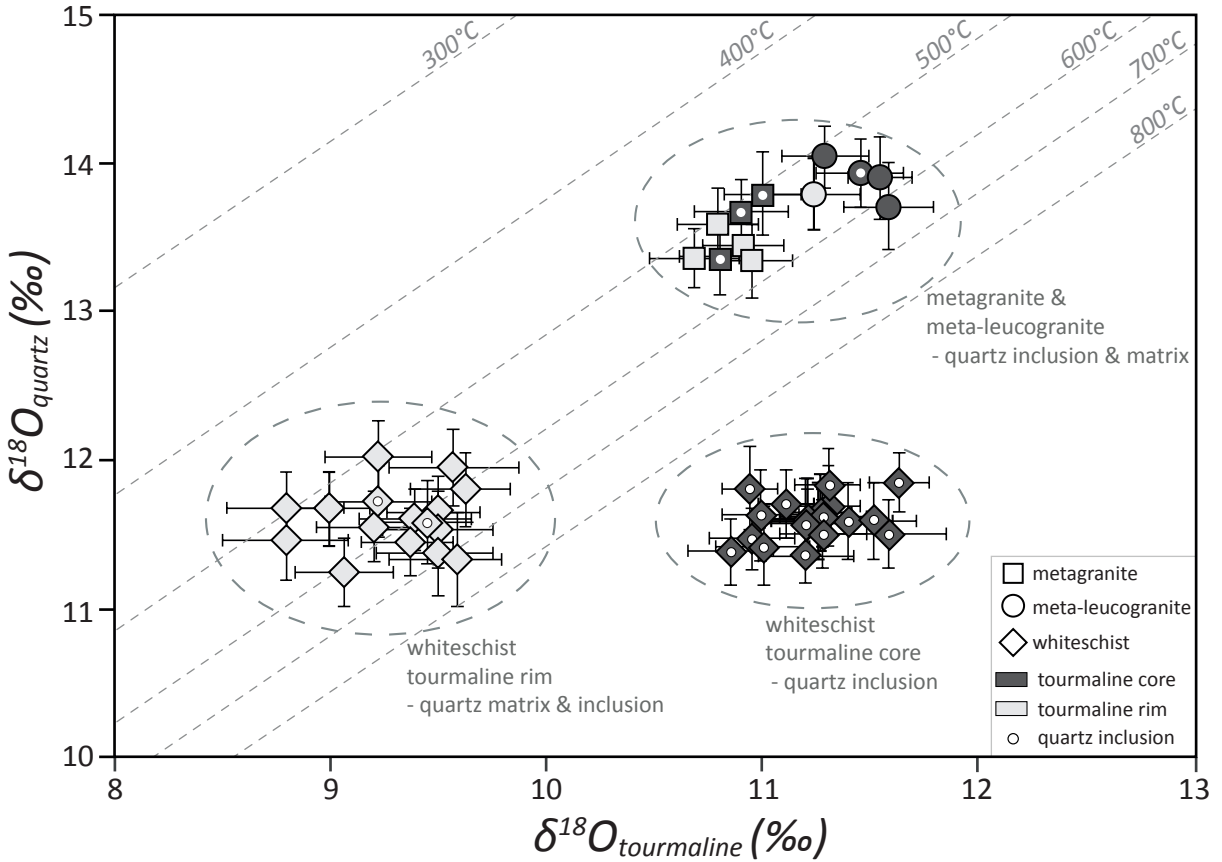
300°C
400°C
500°C
600°C
700°C
800°C
metagranite &
meta-leucogranite
- quartz inclusion & matrix
whiteschist
tourmaline rim
- quartz matrix & inclusion
whiteschist
tourmaline core
- quartz inclusion
metagranite
meta-leucogranite
whiteschist
tourmaline core
tourmaline rim
quartz inclusion
δ18Oquartz (‰)
δ18Otourmaline (‰)
15
14
13
12
11
10
8
9
10
11
12
13

Figure 10

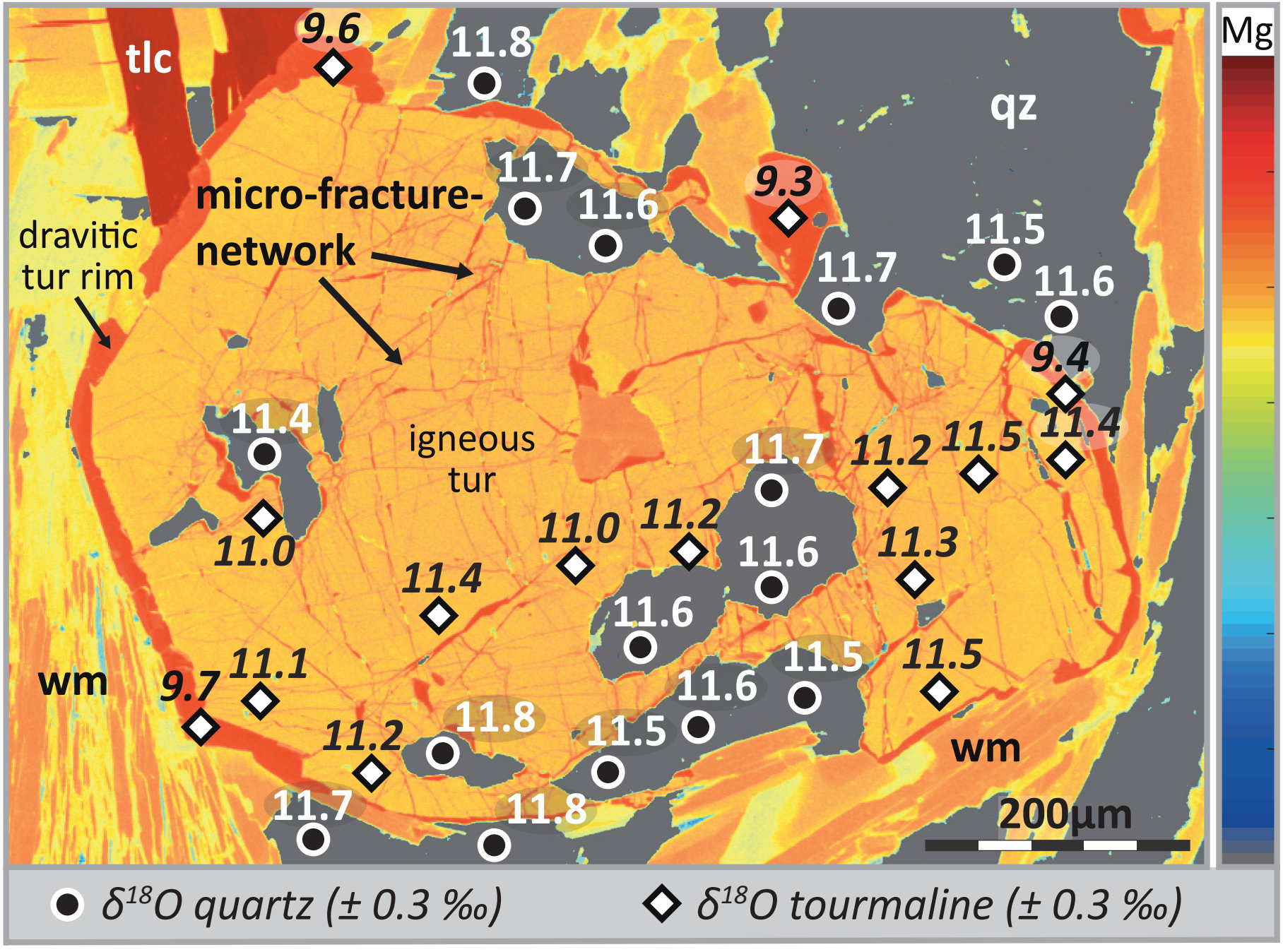
tlc
qz
micro-fracture-network
dravitic tur rim
igneous tur
wm
wm
9.6
11.8
11.7
11.6
9.3
11.5
11.7
11.6
9.4
11.4
11.4
11.0
11.7
11.2
11.5
11.4
11.0
11.2
11.6
11.3
11.6
11.4
11.5
11.5
9.7
11.1
11.6
11.8
11.2
11.5
11.7
11.8
200µm
Mg
δ18O quartz (± 0.3 ‰)
δ18O tourmaline (± 0.3 ‰)

Figure 11

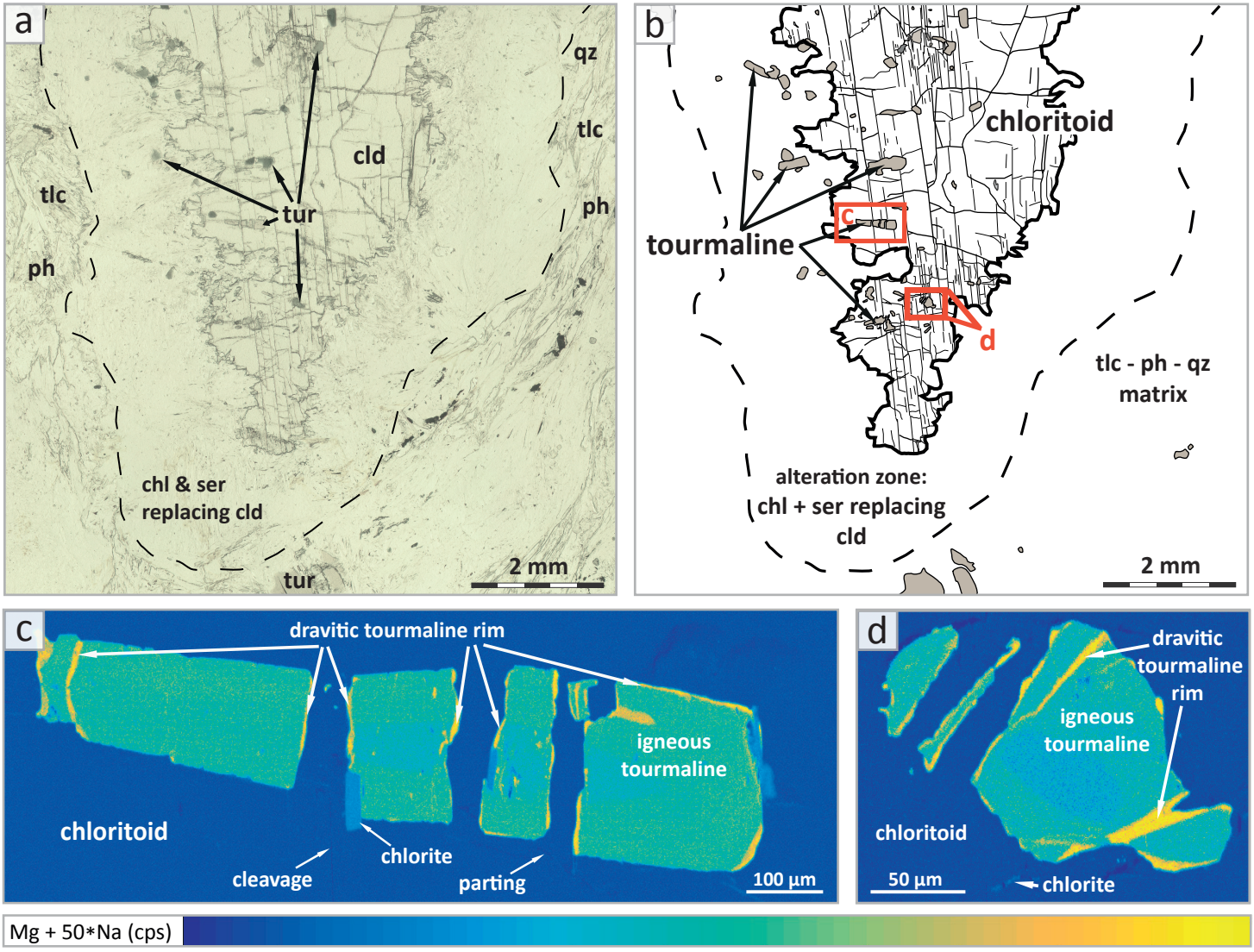
a
qz
tlc
cld
tlc
tur
ph
ph
chl & ser
replacing cld
tur
2 mm
b
chloritoid
c
tourmaline
d
tlc - ph - qz
matrix
alteration zone:
chl + ser replacing
cld
2 mm
c
dravitic tourmaline rim
igneous
tourmaline
chloritoid
chlorite
cleavage
parting
100 µm
d
dravitic
tourmaline
rim
igneous
tourmaline
chloritoid
50 µm
chlorite
Mg + 50*Na (cps)